JACS
JOURNAL OF THE AMERICAN CHEMICAL SOCIETY
pubs.acs.org/JACS
Article

Local Chain Feature Mandated Self-Assembly of Block Copolymers

Zhanhui Gan, Dongdong Zhou, Zhuang Ma, Miao Xu, Zhuoqi Xu, Jiawen He, Jiajia Zhou, and Xue-Hui Dong*

Cite This: J. Am. Chem. Soc. 2023, 145, 487−497
Read Online
ACCESS | Metrics & More | Article Recommendations | Supporting Information

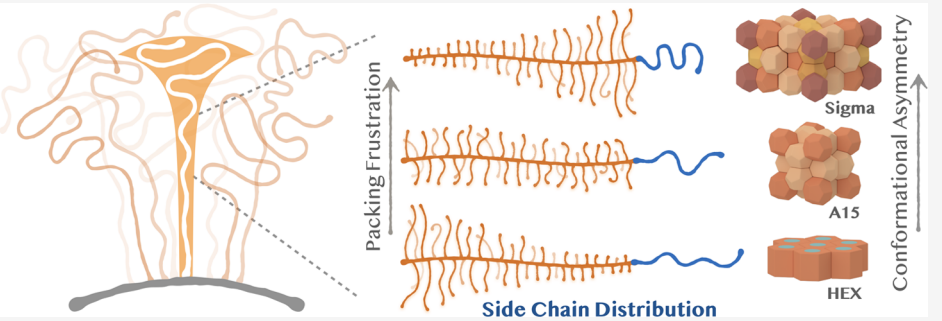

ABSTRACT: This work demonstrates an effective and robust approach to regulate phase behaviors of a block copolymer by programming local features into otherwise homogeneous linear chains. A library of sequence-defined, isomeric block copolymers with globally the same composition but locally different side chain patterns were elaborately designed and prepared through an iterative convergent growth method. The precise chemical structure and uniform chain length rule out all inherent molecular defects associated with statistical distribution. The local features are found to exert surprisingly pronounced impacts on the self-assembly process, which have yet to be well recognized. While other molecular parameters remain essentially the same, simply rearranging a few methylene units among the alkyl side chains leads to strikingly different phase behaviors, bringing about (i) a rich diversity of nanostructures across hexagonally packed cylinders, Frank−Kasper A15 phase, Frank−Kasper σ phase, dodecagonal quasicrystals, and disordered state; (ii) a significant change of lattice dimension; and (iii) a substantial shift of order-to-disorder transition temperature (up to 40 °C). Different from the commonly observed enthalpy-dominated cases, the frustration due to the divergence between the native molecular geometry originating from side chain distribution and the local packing environment mandated by lattice symmetry is believed to play a pivotal role. Engineering the local chain feature introduces another level of structural complexity, opening up a new and effective pathway for modulating phase transition without changing the chemistry or composition.

INTRODUCTION

Packing frustration, which generally refers to a physical state in which not all competing interactions are simultaneously optimized, is ubiquitous in soft matter systems including colloids, liquid crystals, dendrimers, and polymers and provides a generic concept to understand the underlying principles dictating symmetry selection and phase behaviors.[1,2] For example, frustration exists across multiple length scales in block copolymers consisting of chemically incompatible blocks, a canonical self-assembling paradigm.[2] At the molecular scale, frustration arises because the unlike blocks repel each other, while the covalent bonding prevents a macroscopic separation.[3] At the mesoscopic scale, frustration occurs due to the local preference to maintain the native shape of the assembled motifs and the global constraint to uniformly fill the space without voids.[4,5] At an even larger scale, frustration could be induced by external fields and/or spatial confinements.[6] Delicate compromises among these opposite tendencies give rise to thermodynamically stable molecular arrangements. Rational manipulation of packing frustration could effectively alter the free energy landscape, modulating phase behaviors and affording access to complex phases otherwise unattainable (such as Frank−Kasper phases and quasicrystalline phases).[5,7−12] The key point is to establish a quantitative relationship and understand underlying principles.

Thermodynamically, self-assembly of the block copolymer is believed to be dictated by merely a small set of molecular variables, including overall chain length (N), composition (f) describing the relative occupied volume, Flory−Huggins interaction parameter (χ) related to immiscibility between unlike components, and conformational asymmetry quantifying the difference of the segment size of each block ($\varepsilon = b_A^2/$

Received: October 11, 2022
Published: December 26, 2022

https://doi.org/10.1021/jacs.2c10761
J. Am. Chem. Soc. 2023, 145, 487−497

Scheme 1. (a) Schematic Illustration of Segment Distribution of a Random Coil in the Unperturbed State (Left) and a Stretched Chain Tethered on a Surface (or Interface, Right); (b) Bottlebrush Polymers with Different Local Features Experience Varying Degrees of Packing Frustration

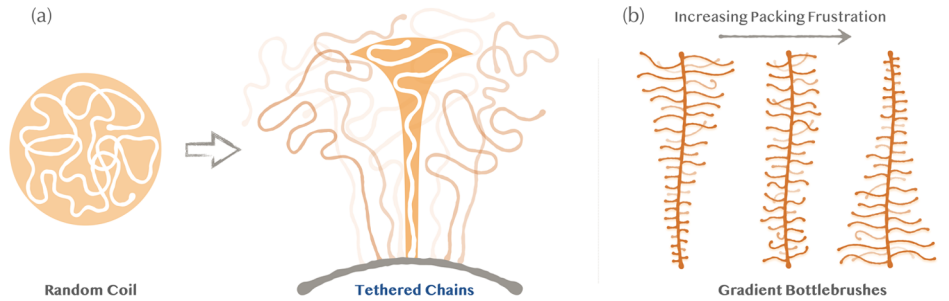

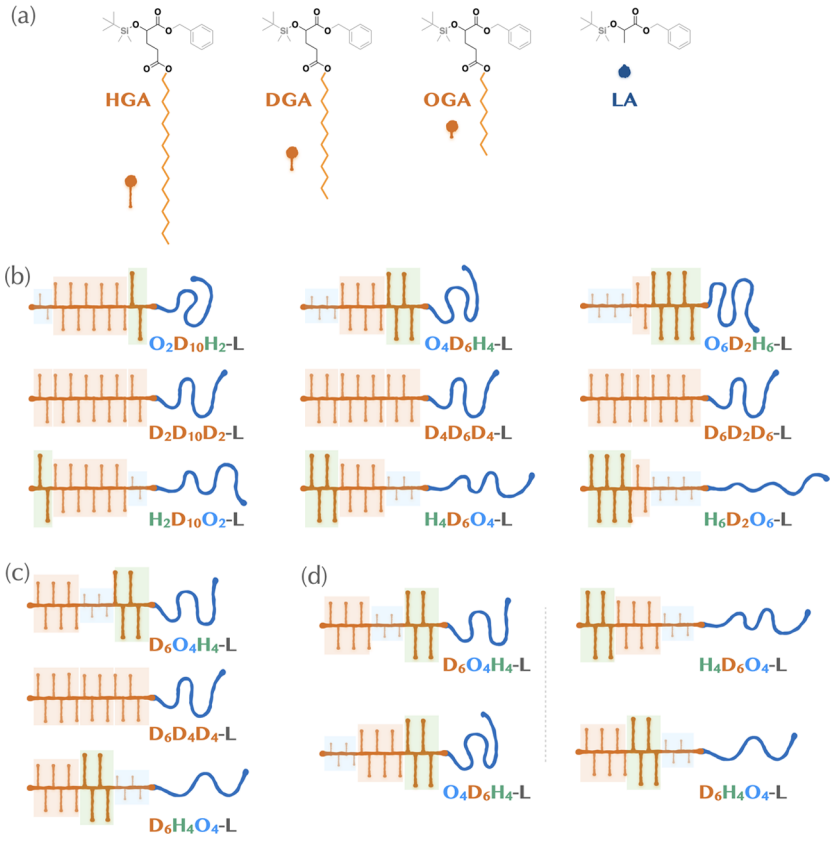

Figure 1. (a) Chemical structure of CGA and LA monomers. (b–d) *o*CGA-*o*LA diblock copolymers with side chain variation at two ends (b), close to the interface (c), and in the distal region (d).

b_B^2).[13−15] Accordingly, packing frustration can be regulated by tuning the interfacial tension using blocks with different segregation strength,[16] by adjusting the relative stretching energy using blocks with dissimilar Kuhn lengths[17−19] or asymmetric architectures,[20−24] or by blending with block copolymers or homopolymers to synergistically fill the polyhedral Voronoi cells.[25−30] Under the mean-field approximation, each constituent block is generally treated as a uniform chain with properties remaining invariant throughout the backbone, while local molecular features are largely averaged out and overlooked.[31] In contrast, *Nature* sets its sights on a much smaller length scale. Through precise regulation of local monomer sequence and stereochemistry, natural polymers are endowed with unparalleled structural and functional complexity using a limited number of simple building blocks. Introducing molecular features into otherwise homogeneous chains is thus expected to greatly expand the parameter space for structural engineering.

Flexible linear polymers are generally abstracted as freely jointed chains consisting of coarse-grained segments uniformly distributed along the backbone. The unconstrained bond orientation leads to random-coil conformation with a uniform segment density. This unperturbed symmetry, however, is broken once a polymer is tethered on a substrate (e.g., polymer brushes) or localized to an interface (e.g., block copolymers) due to the existence of nonequivalent chain ends (free end vs fixed end).[32] With the increase in grafting density, tethered chains are strongly stretched near the substrate/interface while under relaxation at their free ends (Scheme 1a). Whereas a constant overall density is maintained, the segment distribution, however, is significantly skewed toward the free end for each individual chain. This feature is captured by the parabolic

https://doi.org/10.1021/jacs.2c10761
J. Am. Chem. Soc. 2023, 145, 487−497

brush model, in which the segment distribution profile is depicted as a "tree" with a narrow "trunk" tethered on the interface and a broad "crown" at their free ends (Scheme 1a).[33] Spatially pre-programming segment density distribution conforming to a local packing environment into the primary chemical structure would effectively mitigate packing frustration (Scheme 1b). This design principle, however, has yet to be well appreciated and exploited due to the lack of precise and efficient methods to break the intrinsic symmetry of a linear chain.

Recently, it has been demonstrated that geometric features can be encoded by sequential ring-opening metathesis polymerization of macromonomers of different lengths, yielding bottlebrush polymers with well-controlled side-chain length gradients along the backbone.[34−39] The inherent monomer sequence and chain-length heterogeneities associated with statistical growth, however, deteriorate the spatial resolution and hamper quantitative investigations.[39−41] Our group has recently developed a concise and modular model system for constructing discrete polymers with precisely defined side chain patterns.[42] A group of orthogonally protected hydroxyglutaric acid derivatives bearing different hydrocarbon pendants were designed. Iteratively connecting these homologous monomers according to pre-designed sequences generates discrete polymers with exact chemical structure, uniform chain length, and programmable side-chain gradients. In this study, we systematically investigate and highlight the critical contribution of local features to the formation and evolution of nanostructures. A library of sequenced-defined block copolymers with globally the same composition but locally different side chain distribution was designed and prepared. Simply displacing a few methylene units of the side chain leads to remarkably different phase behaviors. The lattice symmetry, domain size, and phase stability of the assembled structures can be effectively regulated. The results explicitly demonstrate that the local chain feature is a robust variable for rational structural manipulation, offering rich potential in tailoring the self-assembly process without changing the composition or chemistry.

RESULTS

Discrete polymers with precise chemical structure and uniform chain length were designed and synthesized using a family of orthogonally protected hydroxyglutaric acid derivatives (CGA, where C stands for hydrocarbon side chains; Figure 1a), following the divergent/convergent strategy reported in our earlier studies.[42] These homologous monomers share similar chemical features, differing only in the size of the side substituents. For convenience, they are abbreviated explicitly according to the pendant alkyl ligands: HGA (H, 1-hexadecyl), DGA (D, 1-dodecyl), and OGA (O, 1-octyl). These monomers can be readily connected following the same chemistry. Briefly, the *tert*-butyldimethylsilyl (TBDMS) and benzyl (Bn) protecting groups can be selectively removed, and the activated hydroxyl/carboxyl functional groups are then coupled through esterification, generating a dimer with the same latent functional groups (Scheme S2).[43−45] Repeating the cycle leads to discrete chains with precise monomer sequence and exact chain length (Figures S1−S4).[46]

Given the same backbone chemistry, the monomer sequence transcribes into diverse local side chain patterns, breaking the intrinsic symmetry and generating distinct molecular geometries. In this study, we rationally designed different side chain features by modularly connecting three types of fragments (H_{n1}, D_{n2}, and O_{n3}) in tandem (i.e., D_n, $H_{n1}D_{n2}O_{n3}$, $O_{n3}D_{n2}H_{n1}$, $D_{n2}H_{n1}O_{n3}$, and $D_{n2}O_{n3}H_{n1}$, where subscripts are the number of repeat units; Schemes S3 and S5), under the premise of constant overall composition ($n = n_1 + n_2 + n_3$, and $n_1 = n_3$). Among them, D_n refers to a polymer chain with a uniform contour along the backbone, while others have varying side chain distributions (Figure 1b−d). Specifically, the $H_{n1}D_{n2}O_{n3}$ and $O_{n3}D_{n2}H_{n1}$ series have monotonically decreasing or increasing gradients, while $D_{n2}H_{n1}O_{n3}$ and $D_{n2}O_{n3}H_{n1}$ series are nonmonotonic (Figure 1b,c). The relative fragment size (n_1, n_2, and n_3) can be further adjusted to finely trim the local feature (Figure 1b). In total, nine isomeric bottlebrush chains with exactly the same composition but varying side chain distributions were prepared in this study (Table 1). The

Table 1. Molecular Characterization of the *o*CGA Chains

sample	MW_{cal}[a]	MW_{obs}[b]	Đ[c]	side chain[d]
D_{14}	4399.15	4421.85	<1.001	uniform
$H_6D_2O_6$	4399.15	4422.63	<1.001	monotonically decreasing
$H_4D_6O_4$		4421.10	<1.001	
$H_2D_{10}O_2$		4422.86	<1.001	
$O_6D_2H_6$	4399.15	4423.65	<1.001	monotonically increasing
$O_4D_6H_4$		4422.11	<1.001	
$O_2D_{10}H_2$		4422.12	<1.001	
$D_6H_4O_4$	4399.15	4423.30	<1.001	nonmonotonic
$D_6O_4H_4$		4423.30	<1.001	

[a]Exact molecular weight, Da. [b]Molecular weight observed by MALDI-ToF MS, $[M + Na]^+$, Da. [c]Dispersity, determined by MALDI-ToF MS. [d]Variation trend of side-chain length from TBDMS to Bn terminal.

sequential fragment extension was fully confirmed by proton nuclear magnetic resonance (^{1}H NMR, Figures S1 and S3), size exclusion chromatography (SEC, Figures S2a and S4a), and matrix-assisted laser desorption/ionization time-of-flight mass spectrometry (MALDI-ToF MS, Figures S2b and S4b). This convergent synthetic approach, in principle, enables the production of discrete macromolecules with any axisymmetric shapes. For clarity and consistency, we define the sequence starting from the TBDMS terminal throughout the study (Scheme S6).

Discrete diblock copolymers were modularly prepared by coupling these *o*CGA blocks with an *oligo* lactide (*o*LA) block (Scheme S4). Despite seemingly similar chemical features, the *o*CGA block and *o*LA block are incompatible and readily undergo phase separation. The polarity of the CGA monomer decreases as the length of the pendant hydrocarbon chain increases. In other words, the longer the side chain, the stronger the segregation strength with *o*LA block (i.e., $\chi_{H/L} > \chi_{D/L} > \chi_{O/L}$).[19] Meanwhile, the bulky side chain reduces the normalized segment length ($b_H < b_D < b_O < b_L$), generating substantial conformational mismatches when conjugated with an *o*LA block ($\varepsilon_{H/L} > \varepsilon_{D/L} > \varepsilon_{O/L}$).[19] In this study, more than 40 discrete diblock copolymers with varying local features were prepared (i.e., D_n-L_m, $H_{n1}D_{n2}O_{n3}$-L_m, $O_{n3}D_{n2}H_{n1}$-L_m, $D_{n2}H_{n1}O_{n3}$-L_m, and $D_{n2}O_{n3}H_{n1}$-L_m; $n = n_1 + n_2 + n_3 = 14$; $n_1 = n_3 = 0, 2, 4, 6$; $m = 24, 26, 28, 30, 32$; Scheme S7 and Table 2), covering a broad parameter space. For each sample, all the resonances in the ^{1}H NMR spectra can be assigned with proper integrals (Figure S5), and the SEC profile shows

https://doi.org/10.1021/jacs.2c10761
J. Am. Chem. Soc. 2023, 145, 487−497

Table 2. Structural Characterization of Discrete Diblock Polymer Isomers with Monotonic Side Chain Gradients

sample	MW (Da)[a]	f_{LA}[b]	phase[c]	a (nm)[d]	D (nm)[e]	T_{ODT}[f]
$O_6D_2H_6$-L_{24}	6128.66	0.248	DIS			
$O_4D_6H_4$-L_{24}			DIS			
D_{14}-L_{24}			DIS			
$H_4D_6O_4$-L_{24}			A15	18.56^3	11.51	
$H_6D_2O_6$-L_{24}			HEX	9.26		35
$O_6D_2H_6$-L_{26}	6272.71	0.263	DIS			
$O_4D_6H_4$-L_{26}			DDQC			
$O_2D_{10}H_2$-L_{26}			DDQC			
D_{14}-L_{26}			σ	$37.09^2 \times 19.62$	11.98	
$H_2D_{10}O_2$-L_{26}			A15	18.81^3	11.67	
$H_4D_6O_4$-L_{26}			HEX	9.33		
$H_6D_2O_6$-L_{26}			HEX	9.41		
$O_6D_2H_6$-L_{28}	6416.75	0.278	σ	$34.85^2 \times 18.37$	11.24	36
$O_4D_6H_4$-L_{28}			σ	$36.50^2 \times 19.24$	11.77	40
$O_2D_{10}H_2$-L_{28}			σ	$36.51^2 \times 19.28$	11.78	50
D_{14}-L_{28}			A15	19.24^3	11.94	50
$H_2D_{10}O_2$-L_{28}			A15	19.75^3	12.25	60
$H_4D_6O_4$-L_{28}			HEX	9.73		
$H_6D_2O_6$-L_{28}			HEX	9.76		75
$O_6D_2H_6$-L_{30}	6560.79	0.292	A15	17.99^3	11.16	50
$O_4D_6H_4$-L_{30}			A15	18.88^3	11.71	55
$O_2D_{10}H_2$-L_{30}			A15	19.24^3	11.94	55
D_{14}-L_{30}			A15	20.51^3	12.72	60
$H_2D_{10}O_2$-L_{30}			HEX	9.82		70
$H_4D_6O_4$-L_{30}			HEX	9.92		85
$H_6D_2O_6$-L_{30}			HEX	9.96		85
$O_6D_2H_6$-L_{32}	6704.83	0.305	A15	18.61^3	11.53	60
$O_4D_6H_4$-L_{32}			A15	19.85^3	12.31	60
$O_2D_{10}H_2$-L_{32}			A15	20.01^3	12.41	65
D_{14}-L_{32}			A15	21.04^3	13.05	65
$H_2D_{10}O_2$-L_{32}			HEX	10.17		85
$H_4D_6O_4$-L_{32}			HEX	10.25		90
$H_6D_2O_6$-L_{32}			HEX	10.33		95

[a]Overall exact molecular weight, Da. [b]Volume fraction of *o*LA block. [c]Phase, determined by SAXS. [d]Lattice dimensions: intercolumn distances of HEX, or lattice parameters of A15 and σ phases. [e]Average diameter of spherical motifs of A15 and σ phases. See the Supporting Information for detailed calculations. [f]Order−disorder transition temperature (°C), determined by in situ SAXS.

unimodal and symmetric elution traces (Figures S9 and S10). Moreover, MALDI-ToF MS displays a single peak with the observed molecular weight in perfect accordance with the calculated value, unambiguously validating the chemical structure in atomic precision (Figures 2, S7, and S8). Molecular information was summarized in Tables 2 and 3, and detailed syntheses can be found in the Supporting Information.

Compared with other generic molecular variables (e.g., volume fraction), the monomer sequence provides unparalleled opportunities to finely regulate the nanostructure and properties. Even a slight local change may affect the overall chain conformation and thus lead to distinct molecular packings. In this study, with elaborately designed isomeric block copolymers, the detailed effects of local sequence on the phase behaviors were quantitatively highlighted with an exceptionally high resolution (Tables 2 and 3). The side chain variation occurs either at two ends (i.e., **HDO**-, **DDD**-, and **ODH**-; Figure 1b), close to the interface (i.e., D**HO**-, D**DD**-, and D**OH**-; Figure 1c), or in the distal region (i.e., **OD**H- and **DO**H-; **HD**O- and **DH**O-; Figure 1d) of the *o*CGA block. Variation of the sequence generates only differences in the side chain gradient, while other parameters remain essentially unchanged. The precise chemistry eliminates all the defects and uncertainties associated with statistical distribution, providing a delicate platform for fundamental inquiries into the role of local chain features. Benefiting from the absence of chain entanglement and low glass transition temperature, ordered structures readily develop with a brief thermal treatment, which were identified by small-angle X-ray scattering (SAXS). The samples were first held at a high temperature (120 °C) for 10 min to erase the thermal history, and then, quenched to room temperature (*ca.* 25 °C). A followed-up annealing process at an elevated temperature (40 °C) promotes the formation of the Frank−Kasper phases, a fascinating family of low-symmetry spherical packings consisting of multiple nonequivalent motifs of different shapes, sizes, and coordination numbers.[7,9,11,47−53] The recent emergence of these complex phases in block copolymer disrupts the long-standing phase principles that body centered cubic is the most prevalent spherical packing.[11]

We first focus on the discrete block copolymers with a D fragment in the middle (i.e., $H_{n1}D_{n2}O_{n3}$-L_m, D_n-L_m, and $O_{n3}D_{n2}H_{n1}$-L_m). By tuning the number of H and O residuals at two ends, a monotonic side chain gradient can be produced. To maintain a constant composition, the H and O fragments

https://doi.org/10.1021/jacs.2c10761
J. Am. Chem. Soc. 2023, 145, 487−497

Figure 2. MALDI-ToF MS of discrete *o*CGA-*o*LA diblock copolymers with varying side chain distributions: m = 26 (a), 28 (b), and 32 (c).

Table 3. Structural Characterization of Discrete Diblock Polymer Isomers with Nonmonotonic Side Chain Gradients

sample	MW (Da)[a]	f_{LA}[b]	phase[c]	a (nm)[d]	D (nm)[e]	T_{ODT}[f]
$D_6O_4H_4$-L_{26}	6272.71	0.263	DDQC			
D_{14}-L_{26}			σ	$37.09^2 \times 19.62$	11.98	
$D_6H_4O_4$-L_{26}			A15	18.41^3	11.42	
$D_6O_4H_4$-L_{28}	6416.75	0.278	A15	18.19^3	11.28	
D_{14}-L_{28}			A15	19.24^3	11.94	
$D_6H_4O_4$-L_{28}			HEX	9.13		
$D_6O_4H_4$-L_{32}	6704.83	0.305	A15	19.67^3	12.20	60
D_{14}-L_{32}			A15	21.04^3	13.05	65
$D_6H_4O_4$-L_{32}			HEX	9.69		80
$O_4D_6H_4$-L_{26}	6272.71	0.263	DDQC			
$D_6O_4H_4$-L_{26}			DDQC			
$D_6H_4O_4$-L_{26}			A15	18.41^3	11.42	
$H_4D_6O_4$-L_{26}			HEX	9.33		
$O_4D_6H_4$-L_{28}	6416.75	0.278	σ	$36.50^2 \times 19.24$	11.77	40
$D_6O_4H_4$-L_{28}			A15	18.19^3	11.28	
$D_6H_4O_4$-L_{28}			HEX	9.13		
$H_4D_6O_4$-L_{28}			HEX	9.73		
$O_4D_6H_4$-L_{32}	6704.83	0.305	A15	19.85^3	12.31	60
$D_6O_4H_4$-L_{32}			A15	19.67^3	12.20	60
$D_6H_4O_4$-L_{32}			HEX	9.69		80
$H_4D_6O_4$-L_{32}			HEX	10.25		90

[a]Overall exact molecular weight, Da. [b]Volume fraction of *o*LA block. [c]Phase, determined by SAXS. [d]Lattice dimensions: intercolumn distances of HEX, or lattice parameters of A15 and σ phases. [e]Average diameter of spherical motifs of A15 and σ phases. See the Supporting Information for detailed calculations. [f]Order−disorder transition temperature (°C), determined by in situ SAXS.

https://doi.org/10.1021/jacs.2c10761
J. Am. Chem. Soc. 2023, 145, 487−497

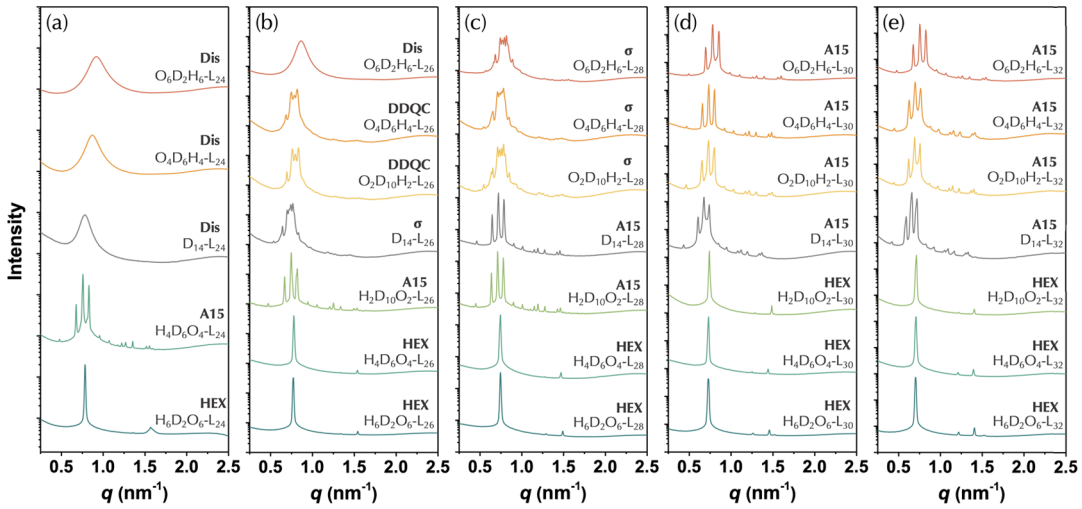

Figure 3. SAXS profiles of discrete block copolymers D_{14}-L_m (gray) and the geometric isomers $H_{n1}D_{n2}O_{n3}$-L_m (green) and $O_{n3}D_{n2}H_{n1}$-L_m (orange): m = 24 (a), 26 (b), 28 (c), 30 (d), and 32 (e). Detailed indexes of the σ and A15 lattice can be found in the Supporting Information. Data are shifted vertically for clarity.

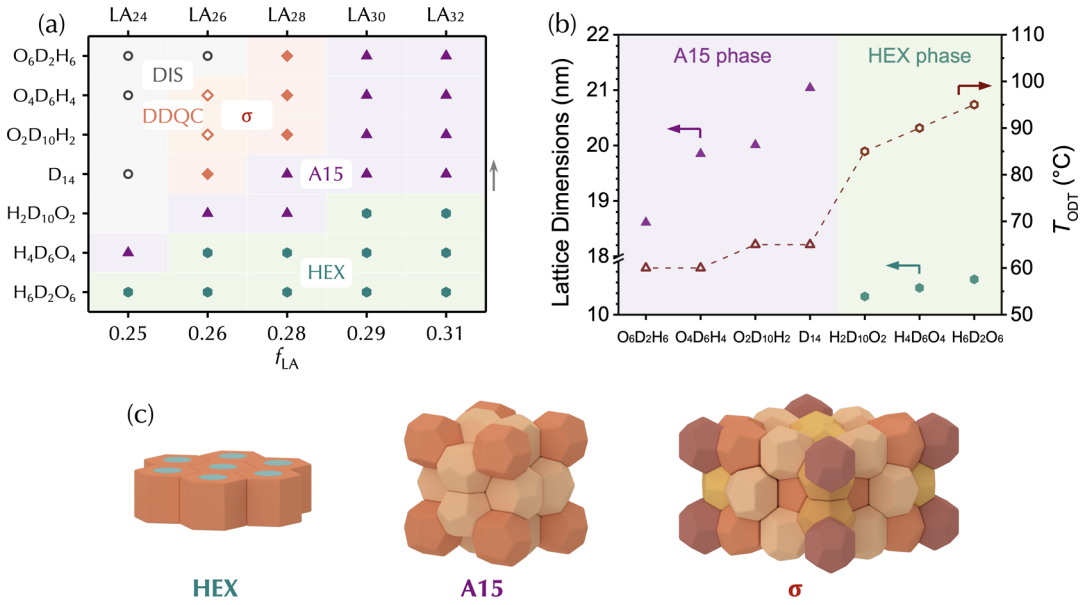

Figure 4. (a) Phase portrait of discrete block copolymers with varying side chain distribution and composition (f_{LA}). (b) Variation of lattice dimension and T_{ODT} of the isomeric species with m = 32. (c) Schematic illustration of typical lattices. The arrow in (a) indicates the increasing direction of conformational asymmetry.

keep the same length ($n_1 = n_3$ = 0, 2, 4, 6). As n_1 increases, the gradient gradually becomes steep (Figure 1b). Despite the subtle chemical structure variation, distinct molecular packings were observed in these isomers (Figure 3). Take a set of isomers with m = 26 as an example (i.e., $H_6D_2O_6$-L_{26}, $H_4D_6O_4$-L_{26}, $H_2D_{10}O_2$-L_{26}, D_{14}-L_{26}, $O_2D_{10}H_2$-L_{26}, $O_4D_6H_4$-L_{26}, and $O_6D_2H_6$-L_{26}; Figure 3b). As a reference, D_{14}-L_{26} with uniform side chains ($n_1 = n_3 = 0$) show signature diffractions with dozens of peaks which perfectly match the pattern of a Frank–Kasper σ lattice ($a = b$ = 37.09 nm, c = 19.62 nm; see Figure S11b for detailed index).[42] For comparison, sample $H_2D_{10}O_2$-L_{26}, of which two butylene units are displaced from the monomers in the vicinity of the interface to those at the terminal side, forms a complex Frank–Kasper A15 structure ($a = b = c$ = 18.81 nm; Figure S11a). Further swapping the side chains ($H_4D_6O_4$-L_{26} and $H_6D_2O_6$-L_{26}) even triggers a transition to the cylindrical phase (HEX; note that the volume fraction is unchanged). In the opposite direction, $O_2D_{10}H_2$-L_{26} and $O_4D_6H_4$-L_{26} with positive gradients adopt the dodecagonal quasicrystal (DDQC) packing, while $O_6D_2H_6$-L_{26} enters the disordered region. Though DDQC is generally considered as a metastable state and would eventually transform to a σ or A15 phase,[48] the stability of the quasicrystal phase in these two cases is significantly enhanced. These DDQC lattices persisted even after annealing at an elevated temperature (40 °C) for more than a few days ($O_2D_{10}H_2$-L_{26} and $O_4D_6H_4$-L_{26}), while a swift transition to Frank–Kasper phases took place within several minutes in the counterparts (D_{14}-L_{26} and $H_2D_{10}O_2$-L_{26}; Figure S12).

The contribution of the local feature under different compositions was studied in parallel (Figure 3). As the number of repeat units of *o*LA block increases, A15 phase appears in the reference diblock copolymers (D_{14}-L_{28}, D_{14}-L_{30}, and D_{14}-L_{32}), following a commonly observed phase

https://doi.org/10.1021/jacs.2c10761
J. Am. Chem. Soc. 2023, 145, 487–497

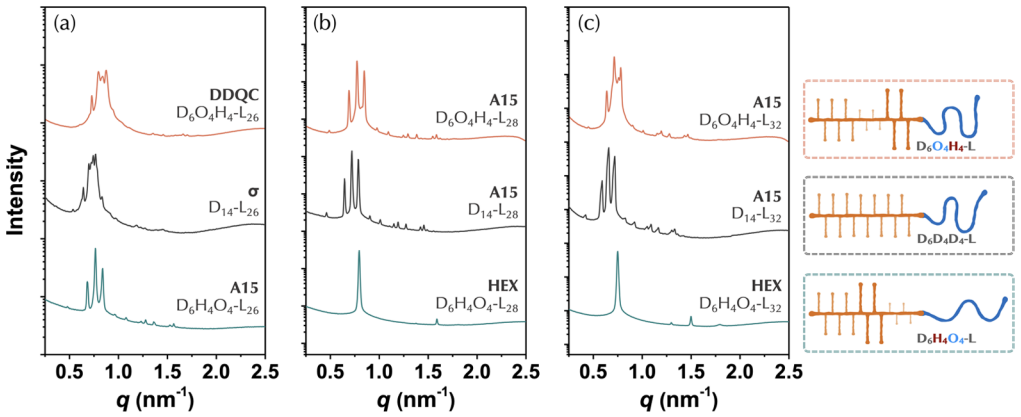

Figure 5. SAXS profiles of discrete block copolymers D_{14}-L_m (black) and the geometric isomers $D_{n2}H_{n1}O_{n3}$-L_m (green) and $D_{n2}O_{n3}H_{n1}$-L_m (orange): m = 26 (a), 28 (b), and 32 (c). Data are shifted vertically for clarity.

progression (Figure 3c–e, gray curves). For each set of isomers, similar structural transitions were recorded as the molecular geometry varies (Figure 4a and Table 2). In general, accommodating the OGA monomer with a shorter side chain close to the interface prompts a transition toward the phase with decreased interfacial curvature (i.e., HEX), while σ phase emerges in the opposite direction (with HGA at the interface). Meanwhile, the side chain gradient also significantly changes the dimension of the lattice, which can be clearly revealed by comparing the isomers adopting the same packing (Figure 4b). The lattice size shrinks as the number of the HGA monomers increases at the junction side, while adding the OGA monomer leads to an opposite change. For example, compared with D_{14}-L_{30} (a = 20.51 nm) and D_{14}-L_{32} (a = 21.04 nm), the A15 lattice of the positively distributed isomers continues to decrease, with more than 10% shrinkage for $O_6D_2H_6$-L_{30} (a = 17.99 nm) and $O_6D_2H_6$-L_{32} (a = 18.61 nm). On the other hand, the intercolumnar distance of the HEX phase gradually expands, as more and more OGA residuals accumulate at the junction point. The structural information was summarized in a phase portrait (Figure 4a). Simply relocating a few methylene units is sufficient to effectively change the phase behaviors, traversing a rich array of nanostructures (HEX → A15 → σ → DDQC → Dis, along perpendicular direction). On the other hand, a substantial change of volume fraction is required to cover this phase region (along the horizontal direction). The results explicitly demonstrated that the local chain feature is a much more effective parameter compared to the compositional variation that is commonly implemented for structural manipulation.[50−53]

Besides the phase structure and the lattice dimension, the side chain distribution also shows a profound influence on phase stability. The order-to-disorder transition temperature (T_{ODT}) is found to be closely related to the local molecular features. Direct evidence comes from the sample set with m = 24 (Figure 3a). While D_{14}-L_{24} and the isomers with positive side chain gradient ($O_4D_6H_4$-L_{24} and $O_6D_2H_6$-L_{24}) remain disordered, the corresponding negatively distributed isomers ($H_4D_6O_4$-L_{24} and $H_6D_2O_6$-L_{24}) assemble into long-range ordered nanostructures under the same condition (A15 and HEX). To acquire more details, temperature-dependent in situ SAXS experiments were performed to measure the transition temperature (Figures S14–S16). Take the samples with m = 32 as an example (Figure S14). For each sample, the scattering peaks progressively broadened upon heating, and ended up with a transition to the disordered state. The transition, however, occurs at quite different temperatures (e.g., 95 °C for $H_6D_2O_6$-L_{32}, 65 °C for D_{14}-L_{32}, and 60 °C for $O_6D_2H_6$-L_{32}, Figure 4b). Similar behaviors were observed in other sets of isomers (Figures S15 and S16). It is also interesting to note that variation of transition temperature is more evident in the sample with negative gradients (HDO-L) than the positive counterparts (ODH-L, Figure S17).

This phenomenon is, however, counter intuitive. The segregation strength between oLA and oCGA blocks progressively decreases as the alkyl pendant shortens (i.e., $\chi_{H/L} > \chi_{D/L} > \chi_{O/L}$), which has been demonstrated in our previous study.[19] It is natural to infer that the isomers with HGA monomers at the diblock joint point should have a higher T_{ODT}, and vice versa. The experimental results, however, reveal an opposite tendency, indicating that the phase stability is determined not only by the enthalpic term to minimize interfacial free energy. Chain conformation and the packing frustration play an indispensable role in the self-assembly process (will be discussed later).

To demonstrate the robustness of the monomer/fragment sequence manipulation, we further investigated the isomeric block copolymers with nonmonotonic side chain distributions. By placing a D_6 fragment at the TBDMS terminal (i.e., $D_6H_4O_4$-L_m, D_{14}-L_m, and $D_6O_4H_4$-L_m, m = 26, 28, and 32), the contribution of a local variation to the phase behaviors was highlighted (Table 3). Compared with the above discussed isomeric species (i.e., $H_4D_6O_4$-L_m and $O_4D_6H_4$-L_m), the side chain variation of this set of samples has been narrowed to the interfacial side, with a much steeper gradient (Figure 1c). Not surprisingly, distinct nanostructures form as the molecular contour varies (Figure 5). For example, compared with D_{14}-L_{26} (σ phase), $D_6H_4O_4$-L_{26} with a negative local gradient adopts the A15 packing, while $D_6O_4H_4$-L_{26} was trapped in the DDQC phase (Figure 5a). Similarly, a transition from A15 to HEX phase, as well as an appreciable difference in lattice dimension, were recorded at other compositions (m = 28 and 32, Figure 5b,c).

On the other hand, one may expect that the effect would attenuate or even vanish when side chain variation occurs distant from the interface. To assess this local effect, we compared another set of elaborately designed molecules (i.e., $D_6H_4O_4$-L_m and $H_4D_6O_4$-L_m; $D_6O_4H_4$-L_m and $O_4D_6H_4$-L_m). The isomers have the same fragment (O_4 or H_4) close to the junction point as a buffer region, with a local variation at the

https://doi.org/10.1021/jacs.2c10761
J. Am. Chem. Soc. 2023, 145, 487−497

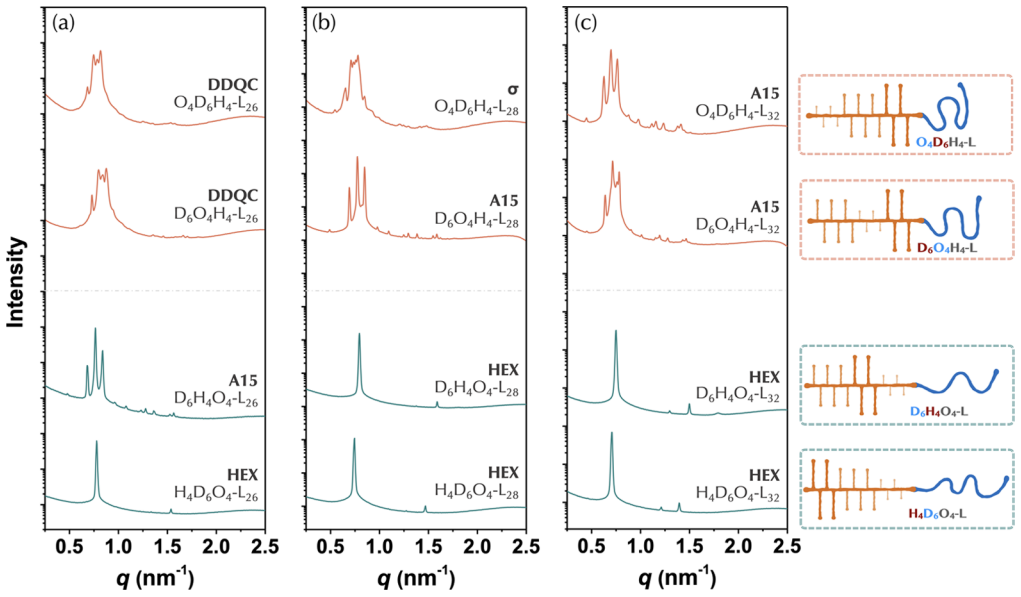

Figure 6. SAXS profiles of the geometric isomers with an O_4 fragment (green) or H_4 fragment (orange) at the interface: m = 26 (a), 28 (b), and 32 (c). Data are shifted vertically for clarity.

far side (Figure 1d and Table 3). It is, however, interesting to recognize that the side chain variation still exerts an appreciable influence on the phase behaviors. Different lattice dimensions or even distinct phase structures were clearly revealed by SAXS profiles (Figure 6). For example, there is a transition from HEX ($H_4D_6O_4$-L_{26}) to the A15 phase ($D_6H_4O_4$-L_{26}), and from A15 ($D_6O_4H_4$-L_{28}) to σ phase ($O_4D_6H_4$-L_{28}) occurring in the molecular pairs with a local sequence reversal. These results highlight the contribution of the seemingly minor change, demonstrating that the subtle variation of the local feature matters.

DISCUSSION

Despite the complex molecular architecture and expanded parameter space, the phase behavior of these block copolymers must comply with the general thermodynamic principles, in which lattice selection is determined by two competing free energy terms, that is, the enthalpic gain (ΔH) due to the decrease of interfacial contact and the entropic penalty (ΔS) associated with unfavored chain stretching and localization of the junction point to the interface.[3,5] Nevertheless, different from most theoretical and experimental studies concerning simple homogeneous chains, both contributions herein are intimately related to the detailed side chain distribution. Given the same composition and backbone chemistry, a local variation would be sufficient to interrupt the free energy landscape, resulting in distinct phase structure, lattice dimension, and phase stability. Though the effect has long been recognized, the inherent imperfections of the primary chemical structure of synthetic polymers, however, overshadow the minute chemical differences. The discrete block copolymers with precisely controlled side chain patterns thus provide an elegant platform to scrutinize the detailed contributions.

Upon phase segregation, the junction points are forced to localize into an interface to minimize unfavored contact, and the tethered blocks resemble generic features of polymer brushes grafted on a substrate.[32] Chains are stretched near the interface, while become relaxed at the free ends (Scheme 1a). A segment (or repeat unit) at distance z from the A/B interface experiences a parabolic potential, $U(z) = K(h^2 - z^2)$, where h is the thickness of the grafted layer.[32] The osmotic pressure within the layer, and thus the energy cost to place a chain unit at a specific position, decreases as z increases. Consequently, introducing local chain features in different regions is expected to generate substantial differences in chain conformation (and thus conformational entropy, Scheme 1b). The translational entropy loss, on the other hand, is nearly identical for all the isomers. It should be noted that the block copolymers in this study are not in the strong segregation limit, and there must exist some deviations from the strict parabolic brush model. Nevertheless, this explicit model can still be applied to qualitatively depict the segmental distribution and the concomitant packing frustration.

Due to asymmetric composition, the minority *o*LA block aggregates to form spherical or cylindrical cores dispersed in the *o*CGA matrix (Figure 4c); the latter can be viewed as being tethered on a convex surface. A chain-end exclusion zone in the vicinity of the convex surface is proposed, in which no free end exists due to overcrowding.[33] In this sense, the contribution of the segments away from the junction point is largely screened, and the interfacial energy is dominated by the monomer pairs directly bonded at the interface ($\Delta H \sim \gamma \Delta S$, where $\gamma \sim \chi^{1/2}$ is the interfacial tension). As discussed above, the segregation strength between *o*LA and *o*CGA blocks progressively decreases as the alkyl pendant shortens (i.e., $\chi_{H/L} > \chi_{D/L} > \chi_{O/L}$), leading to a reduced driving force for phase separation. Compared with the D-L block copolymer, the isomers with HGA fragment at the junction point (ODH-L) should have strong segregation strength to prompt phase separation (and thus a higher T_{ODT} is expected); the situation is reversed for the counterparts with OGA in contact with the *o*LA block (i.e., HDO-L). On the other hand, the elastic deformation depends on the overall side chain arrangement along the backbone. A segment density distribution conforming to a local packing environment (mandated by the lattice symmetry) would effectively alleviate the packing frustration and vice versa. Compared with the reference D-L block copolymer, moving a few methylene segments from the distal

https://doi.org/10.1021/jacs.2c10761
J. Am. Chem. Soc. 2023, 145, 487−497

side (free end) to the interfacial area (i.e., ODH-L) requires extra energy to overcome the osmotic pressure associated with the parabolic potential, and thus destabilizes the phase structure. The larger the pressure, the higher the packing frustration encounters. These two competing tendencies cannot be met simultaneously, and the compromises between the enthalpic and entropic terms determine the phase behaviors.

Experimentally, the isomers with a positive gradient (ODH-L) show a lower T_{ODT} compared with the corresponding D-L block copolymer (Figure S17). On the other hand, the negatively distributed counterparts (HDO-L) are more stable with a higher transition temperature, despite a relatively weak apparent chemical incompatibility. The counter-intuitive results indicate that the entropic contribution plays a dominating role in these geometric isomers. The extra cost of moving chain segments from the distal side to the interface overwhelms the enthalpic gain. Meanwhile, the side chain distribution also has appreciable influences on the grafting density. The bulky HGA fragments experience severe steric hindrance in the vicinity of the interface, demanding a larger inter-chain distance to accommodate the excess side chain units. As more HGA residuals accumulate at the junction region, the interfacial area per chain expands, leading to a reduced dimension along the radial direction (Figure 4b). Following the same reasoning, a larger lattice size is expected in the HDO-L counterparts. The experimental observations are in general consistent with the argument.

The emergence of the unconventional spherical phases is believed to be prompted by a large conformational asymmetry, which quantifies the relative stiffness of the dissimilar blocks ($\varepsilon = b_A^2/b_B^2$, where b_A and b_B are the statistic segment length of the minority and majority components).[17,21] A high conformational mismatch (and thus a stiffer matrix) leads to strong coupling between the shape of the core/corona interface and the shape of the polyhedral Voronoi cell, driving the formation of Frank−Kasper phases.[4] A geometric argument proposed by Bates and co-workers indicates Frank−Kasper phases are desired due to a higher average sphericity.[54] The followed SCFT calculations substantiate the argument and provide deeper insights into the underlying mechanisms.[4,11,55] Very interestingly, the nonuniform side chain brings another level of complexity to the seemingly straightforward scenario. For the blocks with varied local features, the conformational asymmetry is not a simple average over the entire block but rather depends on the spatial distribution. Increasing side-chain length leads to a decreased normalized statistical length b ($b_O > b_D > b_H$).[18] The corona layer is no longer homogeneous throughout the thickness but has *softer* and *stiffer* regions. A block with a monotonically increasing or decreasing side chain distribution can be considered as a spring with a gradual spring constant. Conjugating the minority *o*LA block onto the tight or loose end leads to the divergent capability to transfer the shape of Voronoi cell to the interface and thus distinct phase structures. While no explicit theory is available, it is reasonable to infer that the fragment close to the junction point contributes more to the deformation of the A/B interface, and the contribution gradually decreases as the fragment locating far from the interface. Following this argument, the *effective* conformational asymmetry increases following an order of $H_6D_2O_6$-L_m, $H_4D_6O_4$-L_m, $H_2D_{10}O_2$-L_m, D_{14}-L_m, $O_2D_{10}H_2$-L_m, $O_4D_6H_4$-L_m, and $O_6D_2H_6$-L_m despite the same composition. This sequence is in accordance with the experimental observations that a larger effective conformational asymmetry prefers the Frank−Kasper phases (Figure 4a). Considering the delicate molecular packing, a comprehensive understanding may require intensive numerical calculation or simulation efforts. Given that the discrete copolymers are too short to behave similar to a Gaussian chain, the freely jointed chain might be a better model to capture the salient features.

The arguments were further substantiated by the isomers having nonmonotonic side chain gradients (Figures 5 and 6). A more straightforward case is the isomers with the same fragment (O_4 or H_4) close to the junction point. Despite the existence of a buffer layer, the variation of side chain still exerts an indispensable impact on the phase behaviors, following a similar tendency discussed above. For example, the sample $D_6H_4O_4$-L_{26} with a relatively larger effective conformational asymmetry adopts the A15 packing, while the isomer $H_4D_6O_4$-L_{26} forms a HEX structure (Figure 6a). Moreover, $H_4D_6O_4$-L_{32} has a higher T_{ODT} (90 °C) compared with $D_6H_4O_4$-L_{32} (80 °C). Note that these isomers have the same χ value ($\chi_{H/L}$ or $\chi_{O/L}$), and the observed differences must originate from varying degrees of packing frustration.

CONCLUSIONS

In summary, this work quantitatively scrutinized the influence of local chain features on the phase behaviors using a library of discrete isomeric block copolymers with precise chemical structures and diverse side chain patterns. The phase behaviors are strikingly susceptible to the side chain distribution. A subtle variation is sufficient to interrupt the free energy landscape, resulting in distinct phase structure, lattice dimension, and phase stability. A rich diversity of nanostructures, including cylinders, A15 phase, σ phase, dodecagonal quasicrystals, and disordered state, can be sequentially accessed simply by continuously moving a few methylene units toward the junction side. The packing frustration due to the divergence between the native molecular geometry and the local packing environment dominates the underlying molecular arrangement. Engineering the local chain feature introduces another level of structural complexity, opening up unlimited possibilities for the rational regulation of hierarchical structures.

ASSOCIATED CONTENT

Supporting Information

The Supporting Information is available free of charge at https://pubs.acs.org/doi/10.1021/jacs.2c10761.

Detailed synthetic procedures; additional characterizations; supplementary calculations (PDF)

AUTHOR INFORMATION

Corresponding Author

Xue-Hui Dong − *South China Advanced Institute for Soft Matter Science and Technology, School of Molecular Science and Engineering, South China University of Technology, Guangzhou 510640, China; Guangdong Provincial Key Laboratory of Functional and Intelligent Hybrid Materials and Devices, South China University of Technology, Guangzhou 510640, China;* orcid.org/0000-0002-6395-3103; Email: xdong@scut.edu.cn

https://doi.org/10.1021/jacs.2c10761
J. Am. Chem. Soc. 2023, 145, 487−497

Authors

Zhanhui Gan − *South China Advanced Institute for Soft Matter Science and Technology, School of Molecular Science and Engineering, South China University of Technology, Guangzhou 510640, China;* orcid.org/0000-0002-9646-5747

Dongdong Zhou − *South China Advanced Institute for Soft Matter Science and Technology, School of Molecular Science and Engineering, South China University of Technology, Guangzhou 510640, China; College of Polymer Science and Engineering, State Key Laboratory of Polymer Materials Engineering, Sichuan University, Chengdu 610065, China;* orcid.org/0000-0002-1779-3786

Zhuang Ma − *South China Advanced Institute for Soft Matter Science and Technology, School of Molecular Science and Engineering, South China University of Technology, Guangzhou 510640, China*

Miao Xu − *South China Advanced Institute for Soft Matter Science and Technology, School of Molecular Science and Engineering, South China University of Technology, Guangzhou 510640, China*

Zhuoqi Xu − *South China Advanced Institute for Soft Matter Science and Technology, School of Molecular Science and Engineering, South China University of Technology, Guangzhou 510640, China*

Jiawen He − *South China Advanced Institute for Soft Matter Science and Technology, School of Molecular Science and Engineering, South China University of Technology, Guangzhou 510640, China*

Jiajia Zhou − *South China Advanced Institute for Soft Matter Science and Technology, School of Molecular Science and Engineering, South China University of Technology, Guangzhou 510640, China; Guangdong Provincial Key Laboratory of Functional and Intelligent Hybrid Materials and Devices, South China University of Technology, Guangzhou 510640, China;* orcid.org/0000-0002-2258-6757

Complete contact information is available at: https://pubs.acs.org/10.1021/jacs.2c10761

Author Contributions

The manuscript was written through contributions of all authors. All authors have given approval to the final version of the manuscript.

Notes

The authors declare no competing financial interest.

■ ACKNOWLEDGMENTS

This work was supported by the National Natural Science Foundation of China (22273026 and 51773066) and Guangdong Project (2016ZT06C322). We thank the staffs of Beamline BL16B1 at the Shanghai Synchrotron Radiation Facility (SSRF) for assistance with the SAXS experiments.

■ REFERENCES

(1) Grason, G. M. The Packing of Soft Materials: Molecular Asymmetry, Geometric Frustration and Optimal Lattices in Block Copolymer Melts. *Phys. Rep.* **2006**, *433*, 1−64.

(2) Shi, A.-C. Frustration in Block Copolymer Assemblies. *J. Phys.: Condens. Matter* **2021**, *33*, 253001.

(3) Bates, F. S. Polymer-Polymer Phase Behavior. *Science* **1991**, *251*, 898−905.

(4) Reddy, A.; Buckley, M. B.; Arora, A.; Bates, F. S.; Dorfman, K. D.; Grason, G. M. Stable Frank−Kasper Phases of Self-Assembled, Soft Matter Spheres. *Proc. Natl. Acad. Sci. U.S.A.* **2018**, *115*, 10233.

(5) Reddy, A.; Feng, X.; Thomas, E. L.; Grason, G. M. Block Copolymers Beneath the Surface: Measuring and Modeling Complex Morphology at the Subdomain Scale. *Macromolecules* **2021**, *54*, 9223−9257.

(6) Shi, A.-C.; Li, B. Self-Assembly of Diblock Copolymers Under Confinement. *Soft Matter* **2012**, *9*, 1398−1413.

(7) Kim, K.; Schulze, M. W.; Arora, A.; Lewis, R. M.; Hillmyer, M. A.; Dorfman, K. D.; Bates, F. S. Thermal Processing of Diblock Copolymer Melts Mimics Metallurgy. *Science* **2017**, *356*, 520−523.

(8) Bates, M. W.; Lequieu, J.; Barbon, S. M.; Lewis, R. M.; Delaney, K. T.; Anastasaki, A.; Hawker, C. J.; Fredrickson, G. H.; Bates, C. M. Stability of the A15 Phase in Diblock Copolymer Melts. *Proc. Natl. Acad. Sci. U.S.A.* **2019**, *116*, 13194−13199.

(9) Lee, S.; Bluemle, M. J.; Bates, F. S. Discovery of a Frank-Kasper σ Phase in Sphere-Forming Block Copolymer Melts. *Science* **2010**, *330*, 349−353.

(10) Xie, Q.; Qiang, Y.; Chen, L.; Xia, Y.; Li, W. Synergistic Effect of Stretched Bridging Block and Released Packing Frustration Leads to Exotic Nanostructures. *ACS Macro Lett.* **2020**, *9*, 980−984.

(11) Dorfman, K. D. Frank−Kasper Phases in Block Polymers. *Macromolecules* **2021**, *54*, 10251−10270.

(12) Zhang, C.; Vigil, D. L.; Sun, D.; Bates, M. W.; Loman, T.; Murphy, E. A.; Barbon, S. M.; Song, J.-A.; Yu, B.; Fredrickson, G. H.; Whittaker, A. K.; Hawker, C. J.; Bates, C. M. Emergence of Hexagonally Close-Packed Spheres in Linear Block Copolymer Melts. *J. Am. Chem. Soc.* **2021**, *143*, 14106−14114.

(13) Leibler, L. Theory of Microphase Separation in Block Copolymers. *Macromolecules* **1980**, *13*, 1602−1617.

(14) Matsen, M. W.; Bates, F. S. Unifying Weak- and Strong-Segregation Block Copolymer Theories. *Macromolecules* **1996**, *29*, 1091−1098.

(15) Matsen, M. W.; Bates, F. S. Conformationally Asymmetric Block Copolymers. *J. Polym. Sci., Part B: Polym. Phys.* **1997**, *35*, 945−952.

(16) Sinturel, C.; Bates, F. S.; Hillmyer, M. A. High X−Low N Block Polymers: How Far Can We Go? *ACS Macro Lett.* **2015**, *4*, 1044−1050.

(17) Schulze, M. W.; Lewis, R. M.; Lettow, J. H.; Hickey, R. J.; Gillard, T. M.; Hillmyer, M. A.; Bates, F. S. Conformational Asymmetry and Quasicrystal Approximants in Linear Diblock Copolymers. *Phys. Rev. Lett.* **2017**, *118*, 207801.

(18) Chang, A. B.; Bates, F. S. Impact of Architectural Asymmetry on Frank−Kasper Phase Formation in Block Polymer Melts. *ACS Nano* **2020**, *14*, 11463−11472.

(19) Zhou, D.; Xu, M.; Ma, Z.; Gan, Z.; Zheng, J.; Tan, R.; Dong, X.-H. Discrete Diblock Copolymers with Tailored Conformational Asymmetry: A Precise Model Platform to Explore Complex Spherical Phases. *Macromolecules* **2022**, *55*, 7013−7022.

(20) Grason, G. M.; DiDonna, B. A.; Kamien, R. D. A Geometric Theory of Diblock Copolymer Phases. *Phys. Rev. Lett.* **2003**, *91*, 058304.

(21) Xie, N.; Li, W.; Qiu, F.; Shi, A.-C. σ Phase Formed in Conformationally Asymmetric AB-Type Block Copolymers. *ACS Macro Lett.* **2014**, *3*, 906−910.

(22) Bates, M. W.; Barbon, S. M.; Levi, A. E.; Lewis, R. M.; Beech, H. K.; Vonk, K. M.; Zhang, C.; Fredrickson, G. H.; Hawker, C. J.; Bates, C. M. Synthesis and Self-Assembly of AB_n Miktoarm Star Polymers. *ACS Macro Lett.* **2020**, *9*, 396−403.

(23) Sun, Y.; Tan, R.; Ma, Z.; Gan, Z.; Li, G.; Zhou, D.; Shao, Y.; Zhang, W.-B.; Zhang, R.; Dong, X.-H. Discrete Block Copolymers with Diverse Architectures: Resolving Complex Spherical Phases with One Monomer Resolution. *ACS Cent. Sci.* **2020**, *6*, 1386−1393.

(24) Cai, D.; Li, J.; Ma, Z.; Gan, Z.; Shao, Y.; Xing, Q.; Tan, R.; Dong, X.-H. Effect of Molecular Architecture and Symmetry on Self-Assembly: A Quantitative Revisit Using Discrete ABA Triblock Copolymers. *ACS Macro Lett.* **2022**, *11*, 555−561.

(25) Liu, M.; Qiang, Y.; Li, W.; Qiu, F.; Shi, A.-C. Stabilizing the Frank-Kasper Phases via Binary Blends of AB Diblock Copolymers. *ACS Macro Lett.* **2016**, *5*, 1167−1171.
(26) Li, W.; Duan, C.; Shi, A.-C. Nonclassical Spherical Packing Phases Self-Assembled from AB-Type Block Copolymers. *ACS Macro Lett.* **2017**, *6*, 1257−1262.
(27) Lindsay, A. P.; Lewis, R. M.; Lee, B.; Peterson, A. J.; Lodge, T. P.; Bates, F. S. A15, σ, and a Quasicrystal: Access to Complex Particle Packings via Bidisperse Diblock Copolymer Blends. *ACS Macro Lett.* **2020**, *9*, 197−203.
(28) Cheong, G. K.; Bates, F. S.; Dorfman, K. D. Symmetry Breaking in Particle-Forming Diblock Polymer/Homopolymer Blends. *Proc. Natl. Acad. Sci. U.S.A.* **2020**, *117*, 16764−16769.
(29) Lindsay, A. P.; Cheong, G. K.; Peterson, A. J.; Weigand, S.; Dorfman, K. D.; Lodge, T. P.; Bates, F. S. Complex Phase Behavior in Particle-Forming AB/AB′ Diblock Copolymer Blends with Variable Core Block Lengths. *Macromolecules* **2021**, *54*, 7088−7101.
(30) Ma, Z.; Tan, R.; Gan, Z.; Zhou, D.; Yang, Y.; Zhang, W.; Dong, X.-H. Modulation of the Complex Spherical Packings through Rationally Doping a Discrete Homopolymer into a Discrete Block Copolymer: A Quantitative Study. *Macromolecules* **2022**, *55*, 4331−4340.
(31) Matsen, M. W. The Standard Gaussian Model for Block Copolymer Melts. *J. Phys.: Condens. Matter* **2002**, *14*, R21.
(32) Milner, S. T. Polymer Brushes. *Science* **1991**, *251*, 905−914.
(33) Dimitriyev, M. S.; Grason, G. M. End-Exclusion Zones in Strongly Stretched, Molten Polymer Brushes of Arbitrary Shape. *J. Chem. Phys.* **2021**, *155*, 224901.
(34) Chang, A. B.; Lin, T.-P.; Thompson, N. B.; Luo, S.-X.; Liberman-Martin, A. L.; Chen, H.-Y.; Lee, B.; Grubbs, R. H. Design, Synthesis, and Self-Assembly of Polymers with Tailored Graft Distributions. *J. Am. Chem. Soc.* **2017**, *139*, 17683−17693.
(35) Radzinski, S. C.; Foster, J. C.; Scannelli, S. J.; Weaver, J. R.; Arrington, K. J.; Matson, J. B. Tapered Bottlebrush Polymers: Cone-Shaped Nanostructures by Sequential Addition of Macromonomers. *ACS Macro Lett.* **2017**, *6*, 1175−1179.
(36) Walsh, D. J.; Guironnet, D. Macromolecules with Programmable Shape, Size, and Chemistry. *Proc. Natl. Acad. Sci. U.S.A.* **2019**, *116*, 1538.
(37) Walsh, D. J.; Dutta, S.; Sing, C. E.; Guironnet, D. Engineering of Molecular Geometry in Bottlebrush Polymers. *Macromolecules* **2019**, *52*, 4847−4857.
(38) Ogbonna, N. D.; Dearman, M.; Cho, C.-T.; Bharti, B.; Peters, A. J.; Lawrence, J. Topologically Precise and Discrete Bottlebrush Polymers: Synthesis, Characterization, and Structure−Property Relationships. *JACS Au* **2022**, *2*, 898−905.
(39) Blosch, S. E.; Scannelli, S. J.; Alaboalirat, M.; Matson, J. B. Complex Polymer Architectures Using Ring-Opening Metathesis Polymerization: Synthesis, Applications, and Practical Considerations. *Macromolecules* **2022**, *55*, 4200−4227.
(40) Romio, M.; Grob, B.; Trachsel, L.; Mattarei, A.; Morgese, G.; Ramakrishna, S. N.; Niccolai, F.; Guazzelli, E.; Paradisi, C.; Martinelli, E.; Spencer, N. D.; Benetti, E. M. Dispersity within Brushes Plays a Major Role in Determining Their Interfacial Properties: The Case of Oligoxazoline-Based Graft Polymers. *J. Am. Chem. Soc.* **2021**, *143*, 19067−19077.
(41) Shin, M.; Kim, H.; Park, G.; Park, J.; Ahn, H.; Yoon, D. K.; Lee, E.; Seo, M. Bilayer-Folded Lamellar Mesophase Induced by Random Polymer Sequence. *Nat. Commun.* **2022**, *13*, 2433.
(42) Zhou, D.; Xu, M.; Ma, Z.; Gan, Z.; Tan, R.; Wang, S.; Zhang, Z.; Dong, X.-H. Precisely Encoding Geometric Features into Discrete Linear Polymer Chains for Robust Structural Engineering. *J. Am. Chem. Soc.* **2021**, *143*, 18744−18754.
(43) Takizawa, K.; Tang, C.; Hawker, C. J. Molecularly Defined Caprolactone Oligomers and Polymers: Synthesis and Characterization. *J. Am. Chem. Soc.* **2008**, *130*, 1718−1726.
(44) Tan, R.; Zhou, D.; Liu, B.; Sun, Y.; Liu, X.; Ma, Z.; Kong, D.; He, J.; Zhang, Z.; Dong, X.-H. Precise Modulation of Molecular Weight Distribution for Structural Engineering. *Chem. Sci.* **2019**, *10*, 10698−10705.
(45) Duan, S.; Yang, X.; Yang, Z.; Liu, Y.; Shi, Q.; Yang, Z.; Wu, H.; Han, Y.; Wang, Y.; Shen, H.; Huang, Z.; Dong, X.-H.; Zhang, Z. A Versatile Synthetic Platform for Discrete Oligo- and Polyesters Based on Optimized Protective Groups Via Iterative Exponential Growth. *Macromolecules* **2021**, *54*, 10830−10837.
(46) Liu, Z.; Yang, Z.; Chen, X.; Tan, R.; Li, G.; Gan, Z.; Shao, Y.; He, J.; Zhang, Z.; Li, W.; Zhang, W.-B.; Dong, X.-H. Discrete Giant Polymeric Chains Based on Nanosized Monomers. *JACS Au* **2021**, *1*, 79−86.
(47) Cho, B.-K.; Jain, A.; Gruner, S. M.; Wiesner, U. Mesophase Structure-Mechanical and Ionic Transport Correlations in Extended Amphiphilic Dendrons. *Science* **2004**, *305*, 1598−1601.
(48) Gillard, T. M.; Lee, S.; Bates, F. S. Dodecagonal Quasicrystalline Order in a Diblock Copolymer Melt. *Proc. Natl. Acad. Sci. U.S.A.* **2016**, *113*, 5167−5172.
(49) Percec, V.; Ahn, C.-H.; Ungar, G.; Yeardley, D. J. P.; Möller, M.; Sheiko, S. S. Controlling Polymer Shape Through the Self-Assembly of Dendritic Side-Groups. *Nature* **1998**, *391*, 161−164.
(50) Percec, V.; Imam, M. R.; Peterca, M.; Wilson, D. A.; Graf, R.; Spiess, H. W.; Balagurusamy, V. S. K.; Heiney, P. A. Self-Assembly of Dendronized Triphenylenes into Helical Pyramidal Columns and Chiral Spheres. *J. Am. Chem. Soc.* **2009**, *131*, 7662−7677.
(51) Huang, N.; Imam, M. R.; Sienkowska, M. J.; Peterca, M.; Holerca, M. N.; Wilson, D. A.; Rosen, B. M.; Partridge, B. E.; Xiao, Q.; Percec, V. Supramolecular Spheres Assembled from Covalent and Supramolecular Dendritic Crowns Dictate the Supramolecular Orientational Memory Effect Mediated by Frank-Kasper Phases. *Giant* **2020**, *1*, 100001.
(52) Huang, M.; Hsu, C.-H.; Wang, J.; Mei, S.; Dong, X.-H.; Li, Y.; Li, M.; Liu, H.; Zhang, W.; Aida, T.; Zhang, W.-B.; Yue, S. Z. D.; Cheng, S. Z. D. Selective Assemblies of Giant Tetrahedra via Precisely Controlled Positional Interactions. *Science* **2015**, *348*, 424−428.
(53) Su, Z.; Hsu, C.-H.; Gong, Z.; Feng, X.; Huang, J.; Zhang, R.; Wang, Y.; Mao, J.; Wesdemiotis, C.; Li, T.; Seifert, S.; Zhang, W.; Aida, T.; Huang, M.; Cheng, S. Z. D. Identification of a Frank−Kasper Z Phase from Shape Amphiphile Self-Assembly. *Nat. Chem.* **2019**, *11*, 899−905.
(54) Lee, S.; Leighton, C.; Bates, F. S. Sphericity and Symmetry Breaking in the Formation of Frank−Kasper Phases from One Component Materials. *Proc. Natl. Acad. Sci. U.S.A.* **2014**, *111*, 17723−17731.
(55) Kim, K.; Arora, A.; Lewis, R. M.; Liu, M.; Li, W.; Shi, A.-C.; Dorfman, K. D.; Bates, F. S. Origins of Low-Symmetry Phases in Asymmetric Diblock Copolymer Melts. *Proc. Natl. Acad. Sci. U.S.A.* **2018**, *115*, 847−854.

Supporting Information

Local Chain Feature Mandated Self-assembly of Block Copolymer

Zhanhui Gan,[1] Dongdong Zhou,[1, 3] Zhuang Ma,[1] Miao Xu,[1] Zhuoqi Xu,[1] Jiawen He,[1] Jiajia Zhou,[1,2] and Xue-Hui Dong [1, 2]*

[1]South China Advanced Institute for Soft Matter Science and Technology, School of Molecular Science and Engineering, South China University of Technology, Guangzhou 510640, China

[2]Guangdong Provincial Key Laboratory of Functional and Intelligent Hybrid Materials and Devices, South China University of Technology, Guangzhou 510640, China

[3]College of Polymer Science and Engineering, State Key Laboratory of Polymer Materials Engineering, Sichuan University, Chengdu 610065, China

*Corresponding author: xdong@scut.edu.cn

Table of content

1 Materials and methods

1.1 Chemicals and Solvents

The following chemicals were used as received: D,L-glutamic acid (Adamas, > 98%), 1-hexadecanol (Greagent, > 98%), 1-dodecanol (Adamas, > 98%), 1-octanol (Adamas, > 98%), acetic acid (Greagent, > 99.5%), dcamphorsulfonic acid (TCI, 99%), benzyl alcohol (BnOH, TCI, 99%), meso-lactide (TCI, 85%), benzyl bromide (BnBr, Adamas, 99%), boron trifluoride etherate (BF_3-Et_2O, TCI, 98%), *tert*-butyldimethylsilyl chloride (TBDMSCl, TCI, 98%), imidazole (TCI, 99%), potassium carbonate (K_2CO_3, Greagent, 99.5%), cesium carbonate (Cs_2CO_3, Adamas, 99.9%), palladium on carbon (Pd/C, 10 wt%, Sigma-Aldrich), sodium sulfate (Na_2SO_4, 99+%, General-Reagent), *N*,*N*'-diisopropylcarbodiimide (DIC, Adamas, 98%), 1,4-dioxane (Greagent, > 99.7%), tetrahydrofuran (THF, > 99.5%, Greagent), dichloromethane (CH_2Cl_2, > 99.5%, Greagent), petroleum ether (PE, boiling range 60 °C to 90 °C, Greagent), ethyl acetate (EA, > 99.5%, Greagent), dimethylformamide (DMF, > 99.5%, Greagent), toluene (99%, Guangzhou chemical reagent factory). Anhydrous solvents, including toluene, dimethylformamide (DMF), and dichloromethane (CH_2Cl_2), were obtained with an INERT Pure Solv System (Inert Corporation, USA). 4-(Dimethylamino) pyridinium-4-toluenesulfonate (DPTS) was synthesized according to literature.[1] The CGA monomers were prepared from α-hydroxyglutaric acid following the same procedure as described in our earlier study.

1.2 Instruments and Characterization Methods

Automated column chromatography was performed on SepaBean^{TM} machine T (SanTai Technologies, China) with an automated variable wavelength UV-VIS detector (200-400 nm).

Preparative gel permeation chromatography was conducted on a LaboACE LC-5060 (Japan Analytical Industry Co., Ltd) instrument equipped with two JAIGEL-HR columns (2HR and 2.5HR) in series, a double flow type RI-700 LA detector, and a UV-4ch 800 LA detector. THF was used as eluent with a flowrate of 10 mL/min.

Nuclear magnetic resonance (NMR). All ^{1}H NMR spectra were acquired in a JEOL JNM-ECZR 500 MHz spectrometer with $CDCl_3$ (Cambridge) as a deuterated solvent. The residual proton impurities at δ 7.26 ppm were referenced to $CDCl_3$.

Size exclusion chromatography (SEC). SEC analyses were measured at 40 °C on a Tosoh HLC-8320 instrument equipped with three TSK gel columns (SuperH2000, SuperH3000, and SuperH4000 in series), a double-flow type RI detector, and a UV-8320 UV detector, using THF as eluent. The flow rate was 0.6 mL/min. Data acquisition was performed using EcoSEC software, and molecular weights and molecular weight distributions were calibrated with polystyrene standards (Polymer Laboratories).

Matrix-assisted laser desorption/ionization time-of-flight (MALDI-ToF). MALDI-ToF mass spectroscopy (MS) was acquired on a MALDI SYNAPT G2-Si Mass Spectrometry (Waters). Trans-2-[3-(4-*tert*-butyl-phenyl)-2-methyl-2-propenylidene]-malononitrile (DCTB, Sigma-Aldrich, > 98%) was used as the matrix and prepared in methanol at a concentration of 20 mg/mL. The cationized agent sodium trifluoroacetate was prepared in methanol at a 10 mg/mL concentration. The matrix and cationized salt solutions were mixed in a 10/1 (v/v) ratio. All samples were dissolved in THF with a concentration of 10 mg/mL. During sample preparation, 0.5 μL of the matrix/salt mixture was deposited on microtiter plate wells. After the spots dried, 0.5 μL of sample solution (*ca.* 10 mg/mL in THF) was deposited on the top of a dry matrix/salt spot and added another 0.5 μL of the matrix/salt mixture. After evaporation of the solvent, the target plate was loaded for data collection. The instrument was calibrated prior to measurement with external PS at the molecular weight under consideration. The attenuation of the laser was adjusted to minimize undesired polymer fragmentation and maximize the sensitivity. MassLynx Analysis software was applied to analyze data.

Small angle X-ray scattering (SAXS). SAXS data were collected on Shanghai Synchrotron Radiation (SSRF), beamline BL16B1. The incident X-ray wavelength (λ) was 0.124 nm (photon energy: 10 keV; photo flux: 1×10^{11} phs/s). The beam size was less than 0.4×0.5 mm^2. Scattered X-rays were captured on a 2-dimensional Pilatus detector. The scattering vector (q) was calibrated using a standard of silver behenate with the primary reflection peak at 1.076 nm^{-1}. Different annealing protocols have been applied. In general, samples were heated to above the order-to-disorder transition temperature (120 °C) on a Linkam hot stage for 10 minutes to erase thermal history, and then quenched to room temperature (*ca.* 25 °C). A followed-up annealing process at an elevated temperature (40 °C for 2 h) facilitate the formation of ordered structure. *In-situ* experiments were carried out with a Linkam hot stage mounted onto the SAXS apparatus. Samples were sealed with aluminum foil for good thermal conductivity. The heating rate was 10 °C/min. Samples were equilibrated for 3 minutes at each temperature before

collecting data.

2 Syntheses

2.1 Discrete *o*LA and *o*CGA fragments

2.1.1 Syntheses of discrete *o*LA

All the LA oligomers share the same protecting groups (TBDMS and benzyl) and can be readily connected on demand *via* the iterative convergent growth. Discrete *o*LA (L_m, m = 24, 26, 28, 30, and 32) were synthesized according to the literature (Scheme S1).[2]

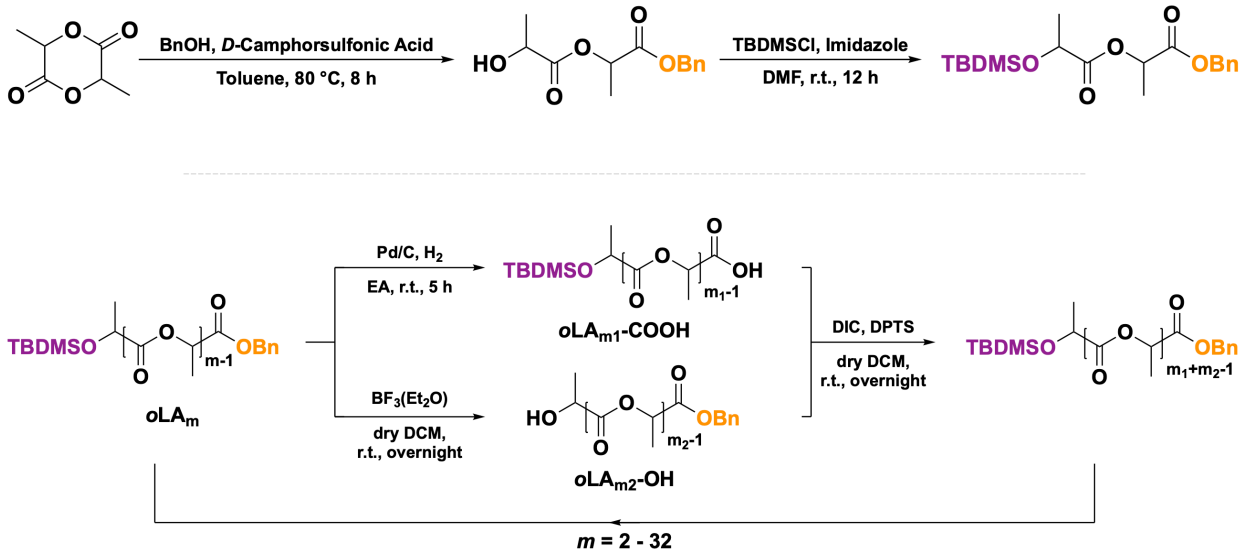

Scheme S1. Synthetic route of orthogonally protected LA monomer (upper) and iterative growth of discrete *o*LA (lower).

2.1.2 Syntheses of discrete *o*CGA fragments

All the CGA monomers share the same protecting groups (TBDMS and benzyl) and can be readily connected on demand *via* the iterative convergent growth. The syntheses of *o*CGA follow our previous work (Scheme S2).[3]

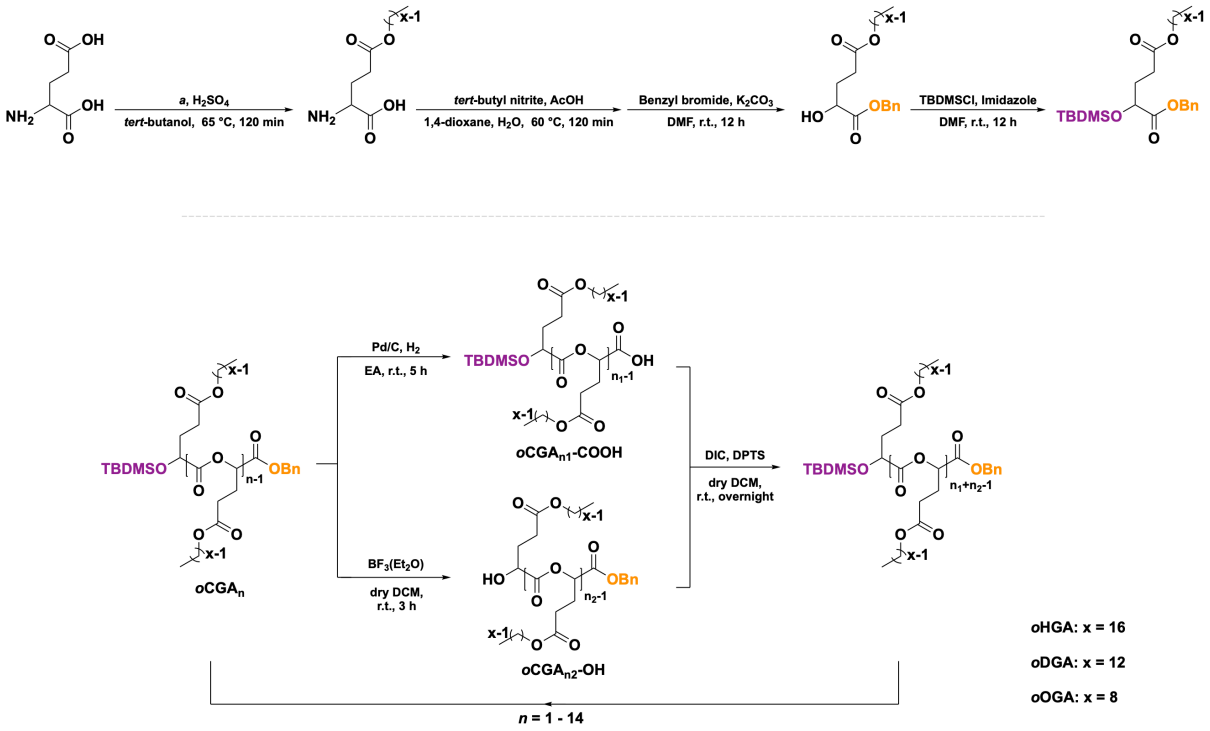

Scheme S2. Synthetic route of orthogonally protected CGA monomer (upper, *a*, 1-octanol for *o*OGA, 1-dodecanol for *o*DGA, and 1-hexadecanol for *o*HGA) and iterative growth of discrete *o*CGA (lower).

2.2 Discrete *o*CGA polymeric isomers with diverse side chain distributions

The syntheses of discrete *o*CGA polymeric isomers followed our previous work, briefly described here.[3] All the *o*CGA fragments share the same protecting groups (*tert*-butyldimethylsilyl, TBDMS, and benzyl, Bn). The protecting groups were selectively removed, and the activated hydroxyl/carboxyl functional groups were coupled through esterification, generating dimers with the same latent functional groups. Repeating the cycle in a particular order led to discrete isomers with designed chain lengths. Take $\mathbf{H_6D_2O_6}$ and $\mathbf{O_6D_2H_6}$ as an example (Scheme S3). Other isomers were obtained following the same procedure.

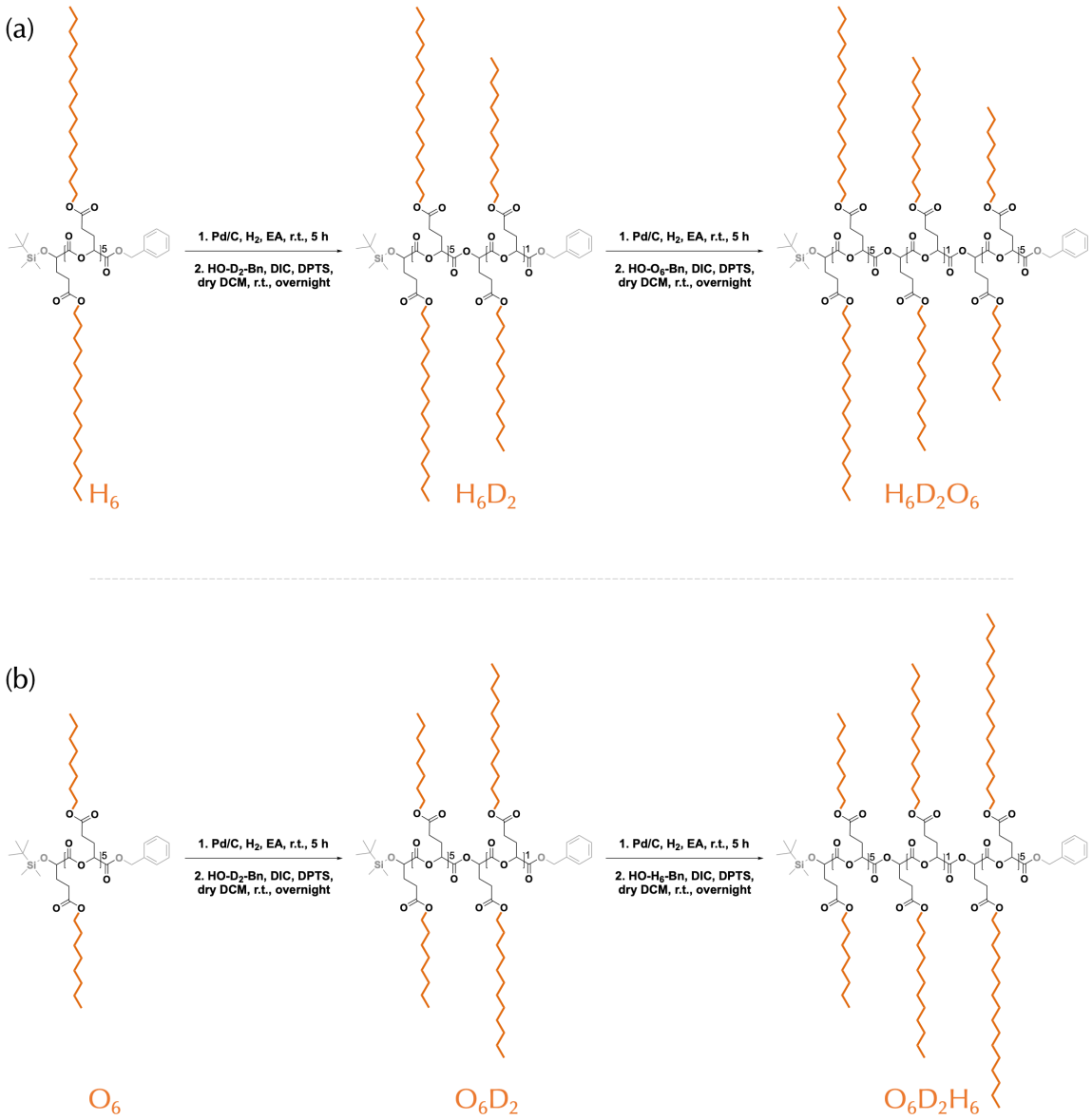

Scheme S3. Synthetic route of discrete *o*CGA polymeric isomers, $H_6D_2O_6$ (a) and $O_6D_2H_6$ (b).

2.2.1 $H_6D_2O_6$

General procedure for the syntheses of TBDMS-*o*CGA$_n$-COOH: Take the **TBDMS-H$_6$-COOH** as an example. TBDMS-H_6-Bn (1.00 g, 0.43 mmol, 1.0 eq) was dissolved in ethyl acetate (60 mL). Then, Palladium (5% on carbon, 20 mg, 0.01 eq of Pd) was added. The mixture was stirred at room temperature under a hydrogen atmosphere for 12 h. The black suspension was filtered through a thick layer of kieselguhr, and the filter cake was washed with EA (3 × 50 mL). After solvent removal, the product (TBDMS-H_6-COOH) was obtained in high purity as a colorless oil (0.88 g, 92% yield) and used directly.

General procedure for the syntheses of OH-*o*CGA$_n$-Bn: Take the **HO-D$_2$-Bn** as an example. TBDMS-D$_2$-Bn (14.5 g, 17.70 mmol, 1.0 eq) was dissolved in 150 mL of anhydrous CH_2Cl_2 with an ice bath. BF_3-etherate (15.0 mL, 88.5 mmol, 5 eq) was then slowly dropped into the solvent above. The mixture was allowed to return to room temperature and was further stirred for 2 h. After TLC showed the reaction was complete, the reaction was quenched by pouring into a saturated aqueous solution of $NaHCO_3$ (200 mL). The resulting organic phase was washed with deionized water (3 × 150 mL) and dried with anhydrous Na_2SO_4. After solvent removal, the crude product was purified by automated column chromatography using PE/EA (95/5 to 85/15, *v*/*v*) as eluent, giving the pure product HO-D$_2$-Bn (10.30 g, 97% yield) as a colorless oil.

Synthesis of H_6D_2. HO-D$_2$-Bn (0.22 g, 0.31 mmol, 1.0 eq), TBDMS-H$_6$-COOH (0.88 g, 0.39 mmol, 1.25 eq), and DPTS (0.018 g, 0.06 mmol, 0.2 eq) were dissolved in 20 mL dried DCM. DIC (0.5 mL) was then slowly dropped into the above solution with an ice bath. The mixture was stirred at room temperature overnight. After removing the excess solvent, the crude product was purified by automated column chromatography with an eluent mixed PE and EA (95/5 to 92/8, *v*/*v*), yielding the product TBDMS-H$_6$D$_2$-Bn as a colorless oil (0.78 g, 85% yield). ^{1}H-NMR ($CDCl_3$, 500 MHz): δ 7.37-7.29 (m, 5H), 5.23 (s, 2H), 5.16 (t, 7H), 4.39-4.35 (m, 1H), 4.05 (t, 16H), 2.62-2.37 (br, 16H), 2.37-2.06 (m, 14H), 2.01 (p, 2H), 1.67-1.57 (br, 16H), 1.36-1.21 (br, 192H), 0.88 (p, 33H), 0.06 (p, 6H). MS (MALDI-TOF, m/z): $[M+Na]^+$ Cal 2968.23; Obs 2969.57.

Synthesis of $H_6D_2O_6$. After the general procedure of deprotection, HO-O$_6$-Bn and TBDMS-H$_6$D$_2$-COOH were obtained. HO-O$_6$-Bn (0.24 g, 0.15 mmol, 1.0 eq), TBDMS-H$_6$D$_2$-COOH (0.54 g, 0.19 mmol, 1.25 eq), and DPTS (0.054 g, 0.03 mmol, 0.2 eq) were dissolved in 10 mL dried DCM. DIC (0.5 mL) was then slowly dropped into the above solution with an ice bath. The mixture was stirred at room temperature overnight. After removing the excess solvent, the crude product was purified by automated column chromatography with an eluent mixed PE and EA (95/5 to 92/8, *v*/*v*). The crude product was further purified by recycling preparative HPLC, yielding the product TBDMS-H$_6$D$_2$O$_6$-Bn as a colorless oil (0.35 g, 52% yield). ^{1}H-NMR ($CDCl_3$, 500 MHz): δ 7.37-7.29 (m, 5H), 5.23 (s, 2H), 5.16 (t, 13H), 4.39-4.35 (m, 1H), 4.05 (t, 28H), 2.62-2.37 (br, 28H), 2.37-2.06 (m, 26H), 2.01 (p, 2H), 1.67-1.57 (br, 28H), 1.36-1.21 (br, 252H), 0.88 (p, 51H), 0.06 (p, 6H). MS (MALDI-TOF, m/z): $[M+Na]^+$ Cal 4422.14; Obs 4422.63.

2.2.2 $O_6D_2H_6$

Synthesis of O_6D_2. After the general procedure of deprotection, HO-D_2-Bn and TBDMS-O_6-COOH were obtained. HO-D_2-Bn (0.35 g, 0.50 mmol, 1.0 eq), TBDMS-O_6-COOH (1.00 g, 0.60 mmol, 1.2 eq), and DPTS (0.03 g, 0.1 mmol, 0.2 eq) were dissolved in 20 mL dried DCM. DIC (0.5 mL) was then slowly dropped into the above solution with an ice bath. The mixture was stirred at room temperature overnight. After removing the excess solvent, the crude product was purified by automated column chromatography with an eluent mixed PE and EA (95/5 to 88/12, *v*/*v*), yielding the product TBDMS-O_6D_2-Bn as a colorless oil (1.0 g, 85% yield). ^{1}H-NMR ($CDCl_3$, 500 MHz): δ 7.37-7.29 (m, 5H), 5.23 (s, 2H), 5.16 (t, 7H), 4.39-4.35 (m, 1H), 4.05 (t, 16H), 2.62-2.37 (br, 16H), 2.37-2.06 (m, 14H), 2.01 (p, 2H), 1.67-1.57 (br, 16H), 1.36-1.21 (br, 96H), 0.88 (p, 33H), 0.06 (p, 6H). MS (MALDI-TOF, m/z): $[M+Na]^+$ Cal 2295.48; Obs 2295.76.

Synthesis of $O_6D_2H_6$. After the general procedure of deprotection, HO-H_6-Bn and TBDMS-O_6D_2-COOH were obtained. HO-H_6-Bn (0.49 g, 0.31 mmol, 1.0 eq), TBDMS-O_6D_2-COOH (0.87 g, 0.4 mmol, 1.29 eq), and DPTS (0.018 g, 0.062 mmol, 0.2 eq) were dissolved in 10 mL dried DCM. DIC (0.5 mL) was then slowly dropped into the above solution with an ice bath. The mixture was stirred at room temperature overnight. After removing the excess solvent, the crude product was purified by automated column chromatography with an eluent mixed PE and EA (95/5 to 92/8, *v*/*v*). The crude product was further purified by recycling preparative HPLC, yielding the product TBDMS-$O_6D_2H_6$-Bn as a colorless oil (0.85 g, 72% yield). ^{1}H-NMR ($CDCl_3$, 500 MHz): δ 7.37-7.29 (m, 5H), 5.23 (s, 2H), 5.16 (t, 13H), 4.39-4.35 (m, 1H), 4.05 (t, 28H), 2.62-2.37 (br, 28H), 2.37-2.06 (m, 26H), 2.01 (p, 2H), 1.67-1.57 (br, 28H), 1.36-1.21 (br, 252H), 0.88 (p, 51H), 0.06 (p, 6H). MS (MALDI-TOF, m/z): $[M+Na]^+$ Cal 4422.14; Obs 4423.65.

2.3 Discrete diblock polymeric structural isomers

With the *o*CGA building blocks, a library of diblock isomers was modularly constructed by conjugating *o*LA blocks through esterification. Take **$H_6D_2O_6$-L*m*** and **$O_6D_2H_6$-L*m*** as an example. Other isomers were obtained following the same procedure.

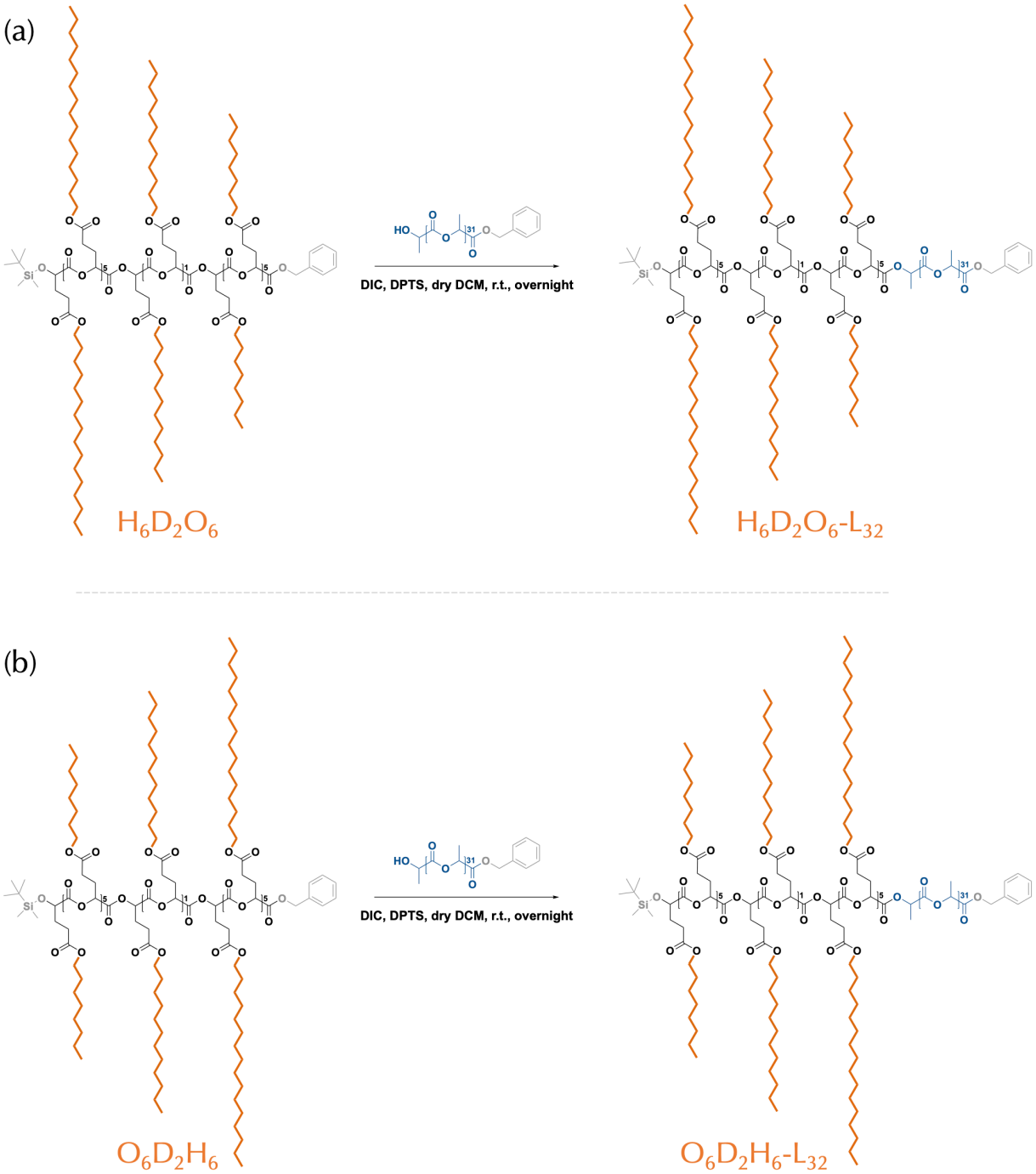

Scheme S4. Synthetic route of discrete diblock polymeric structural isomers, $H_6D_2O_6$-L_{32} (a) and $O_6D_2H_6$-L_{32} (b).

General procedure for the syntheses of OH-*o*LA$_m$-Bn: Take the **HO-L$_{32}$-Bn** as an example. TBDMS-L_{32}-Bn (1.10 g, 0.44 mmol, 1.0 eq) was dissolved in 20 mL of anhydrous CH_2Cl_2 with an ice bath. BF_3-etherate (0.6 mL, 2.2 mmol, 5.0 eq) was then slowly dropped into the solvent above. The mixture was allowed to return to room temperature and was further stirred for 7 h. After TLC showed the reaction was

quenched by pouring into a saturated aqueous solution of $NaHCO_3$ (10 mL). The resulting organic phase was washed with deionized water (3 × 10 mL) and dried with anhydrous Na_2SO_4. After solvent removal, the crude product was purified by automated column chromatography using DCM/EA (90/10 to 60/40, *v*/*v*) as eluent, giving the pure product HO-L_{32}-Bn (1.00 g, 95% yield) as a colorless oil.

General procedure for the syntheses of $H_6D_2O_6$-L_m: Take the **$H_6D_2O_6$-L_{32}** as an example. After the general procedure of deprotection, HO-L_{32}-Bn and TBDMS-$H_6D_2O_6$-COOH were obtained. TBDMS-$H_6D_2O_6$-COOH (40 mg, 0.009 mmol, 1.0 eq), HO-L_{32}-Bn (44 mg, 0.018 mmol, 2.0 eq), and DPTS (1 mg, 0.003 mmol, 0.3 eq) were dissolved in 5 mL dried DCM. DIC (0.5 mL) was then slowly dropped into the above solution with an ice bath. The mixture was stirred at room temperature overnight. The crude product was purified by recycling preparative HPLC, yielding the product TBDMS-$H_6D_2O_6$-L_{32} as a colorless oil (29 mg, 47% yield). ^{1}H-NMR ($CDCl_3$, 500 MHz): δ 7.37-7.29 (m, 5H), 5.23 (s, 2H), 5.16 (t, 45H), 4.39-4.35 (m, 1H), 4.05 (t, 28H), 2.62-2.37 (br, 28H), 2.37-2.06 (m, 26H), 2.01 (p, 2H), 1.67-1.57 (br, 28H), 1.55 (d, 96H), 1.36-1.21 (br, 252H), 0.88 (p, 51H), 0.06 (p, 6H). MS (MALDI-TOF, m/z): $[M+Na]^+$ Cal 6727.82; Obs 6727.16.

General procedure for the syntheses of $O_6D_2H_6$- L_m: Take the **$O_6D_2H_6$-L_{32}** as an example. After the general procedure of deprotection, HO-L_{32}-Bn and TBDMS-$O_6D_2H_6$-COOH were obtained. TBDMS-$O_6D_2H_6$-COOH (65 mg, 0.015 mmol, 1.0 eq), HO-L_{32}-Bn (72 mg, 0.03 mmol, 2.0 eq), and DPTS (1 mg, 0.003 mmol, 0.2 eq) were dissolved in 5 mL dried DCM. DIC (0.5 mL) was then slowly dropped into the above solution with an ice bath. The mixture was stirred at room temperature overnight. The crude product was purified by recycling preparative HPLC, yielding the product TBDMS-$O_6D_2H_6$-L_{32} as a colorless oil (53 mg, 53% yield). ^{1}H-NMR ($CDCl_3$, 500 MHz): δ 7.37-7.29 (m, 5H), 5.23 (s, 2H), 5.16 (t, 45H), 4.39-4.35 (m, 1H), 4.05 (t, 28H), 2.62-2.37 (br, 28H), 2.37-2.06 (m, 26H), 2.01 (p, 2H), 1.67-1.57 (br, 28H), 1.55 (d, 96H), 1.36-1.21 (br, 252H), 0.88 (p, 51H), 0.06 (p, 6H). MS (MALDI-TOF, m/z): $[M+Na]^+$ Cal 6727.82; Obs 6727.16.

3 Supplementary Calculation and Discussion

3.1 The calculation of volume fraction (f_{LA})

The volume fraction of *o*LA component (f_{LA}) is determined by Eq. S1:

$$f_{LA} = \frac{M_L/\rho_L}{M_L/\rho_L + \sum_{i=1}^{14}\left(M_{Ci}/\rho_{Ci}\right)} \tag{S1}$$

where M_L and M_C are the molecular weight of *o*LA and *o*CGA; ρ_L and ρ_C are the densities, respectively; i is the sequence number of *o*CGA monomers from the TBDMS group to the Bn terminal. According to literature[3], ρ_{LA} = 1.25 g/cm^3, ρ_{OGA} = 1.076 g/cm^3, ρ_{DGA} = 1.041 g/cm^3, ρ_{HGA} = 1.008 g/cm^3.

3.2 The characteristic dimension of phases (*a*)

$$\begin{aligned} a &= 2d_{10}/\sqrt{3} && \text{for HEX} \\ a &= 2d_{200} && \text{for A15} \\ a &= \sqrt{17}d_{410};\ c = 2d_{002} && \text{for σ phase} \end{aligned} \tag{S2}$$

3.3 The average diameter of spherical motifs of A15 and σ phases (*D*)

$$\begin{aligned} \langle D\rangle &= \sqrt[3]{\frac{3}{4\pi}}a && \text{for A15} \\ \langle D\rangle &= \sqrt[3]{\frac{V}{5\pi}} && \text{for σ phase} \end{aligned} \tag{S3}$$

where a is the cubic lattice parameter of A15, and V ($V = a * a * c$) is the lattice volume of σ phase.

3.4 Index of peaks in the SAXS pattern of $H_2D_{10}O_2$-L_{26} (A15 phase)

Peak No.	(*hkl*)	$q_{cal.}$ (nm^{-1})	$q_{obs.}$ (nm^{-1})	Peak No.	(*hkl*)	$q_{cal.}$ (nm^{-1})	$q_{obs.}$ (nm^{-1})
1	110	0.472	0.472	**9**	321	1.250	1.250
2	200	0.668	0.668	**10**	400	1.336	1.336
3	210	0.746	0.747	**11**	410	1.377	1.377
4	211	0.818	0.818	**12**	330	1.414	1.417
5	220	0.945	0.945	**13**	411	1.414	1.417
6	310	1.055	1.056	**14**	420	1.494	1.494
7	222	1.158	1.157	**15**	421	1.530	1.531
8	320	1.205	1.204	**16**	332	1.567	1.567

3.5 Index of peaks in the SAXS pattern of $O_6D_2H_6$-L_{28} (σ phase)

Peak No.	(*hkl*)	$q_{cal.}$ (nm^{-1})	$q_{obs.}$ (nm^{-1})	Peak No.	(*hkl*)	$q_{cal.}$ (nm^{-1})	$q_{obs.}$ (nm^{-1})
1	110	0.255		**17**	410	0.743	0.743
2	200	0.361		**18**	330	0.765	0.765
3	101	0.387		**19**	202	0.773	
4	210	0.403		**20**	212	0.794	0.794

5	111	0.427		**21**	411	0.818	0.818
6	220	0.510		**22**	331	0.838	0.836
7	211	0.529		**23**	222	0.853	
8	310	0.570	0.570	**24**	421	0.876	
9	221	0.614	0.614	**25**	312	0.890	0.889
10	301	0.640		**26**	510	0.919	0.917
11	320	0.650		**27**	322	0.944	0.943
12	311	0.665	0.665	**28**	431	0.964	
13	002	0.684	0.684	**29**	501	0.964	0.963
14	400	0.721		**30**	511	0.981	0.980
15	112	0.730		**31**	521	1.029	1.029
16	321	0.734		**32**	432	1.131	

4 Supplementary Schemes and Figures

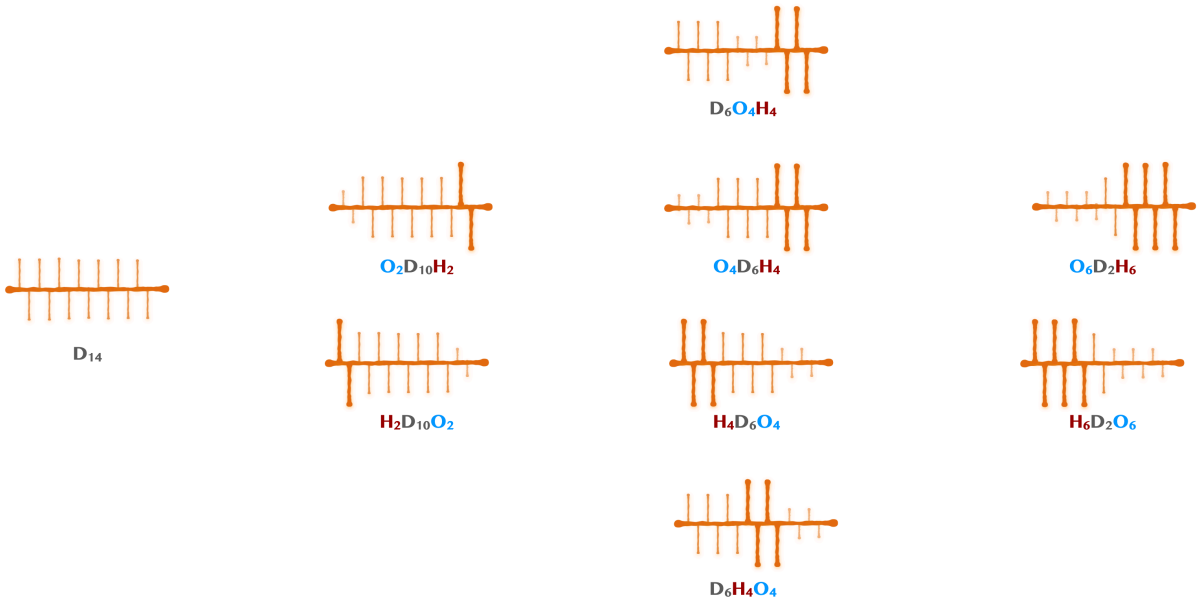

Scheme S5. Schematic illustration of the *o*CGA isomers with different side chain distributions.

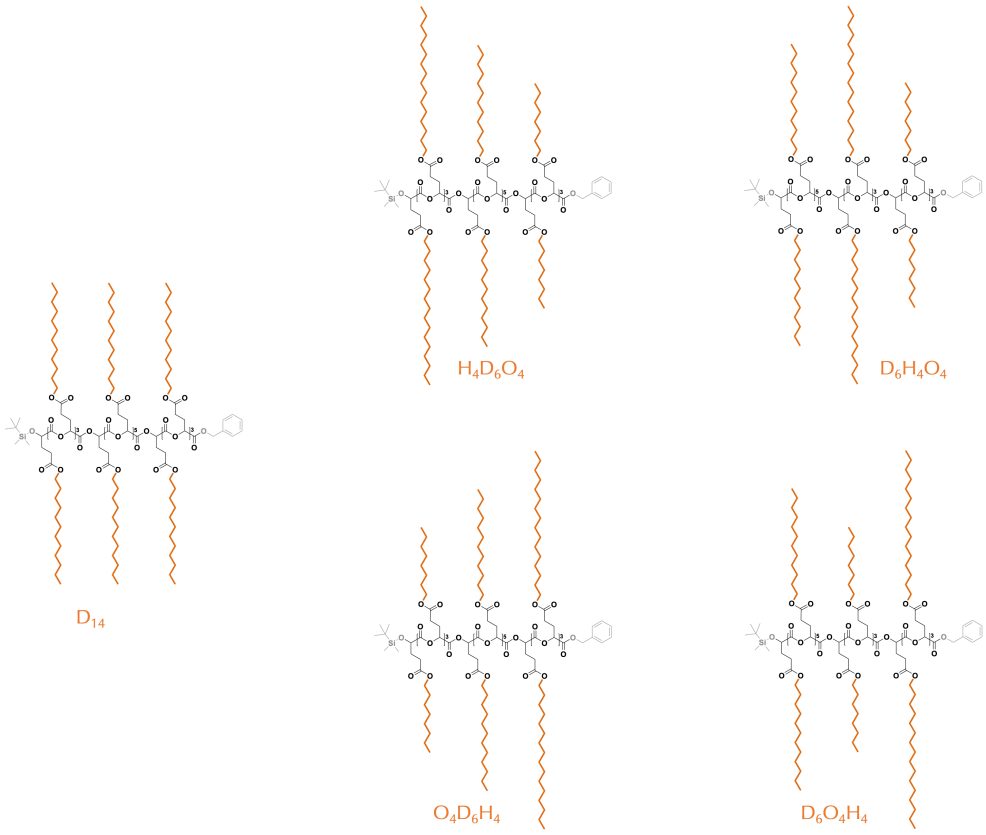

Scheme S6. Typical examples of detailed chemical structures of discrete *o*CGA isomers.

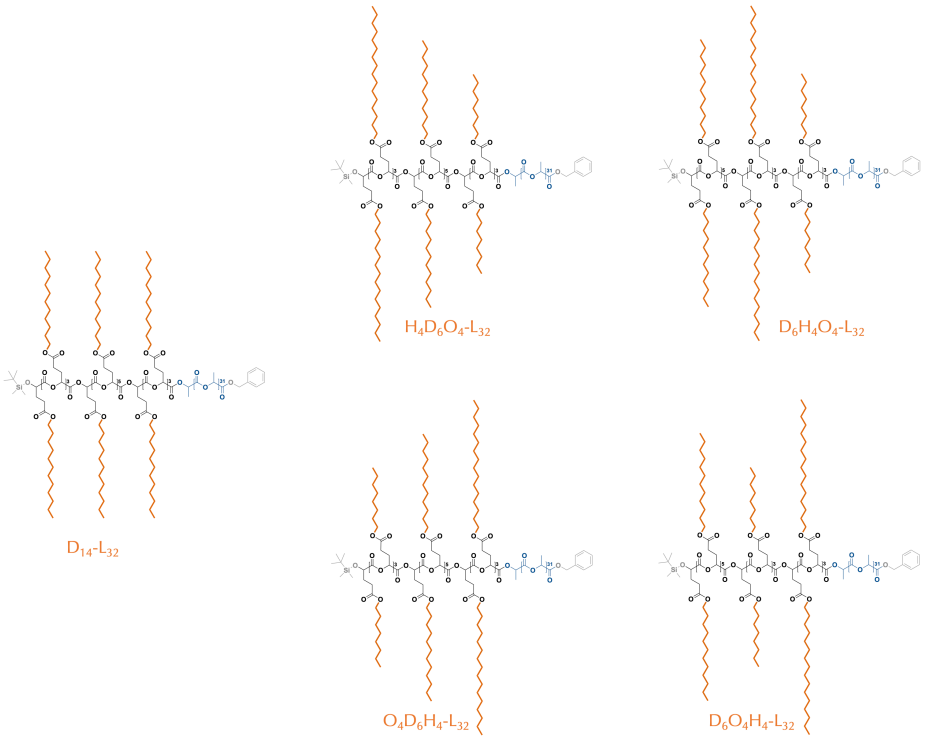

Scheme S7. Typical examples of detailed chemical structures of discrete diblock polymeric structural isomers.

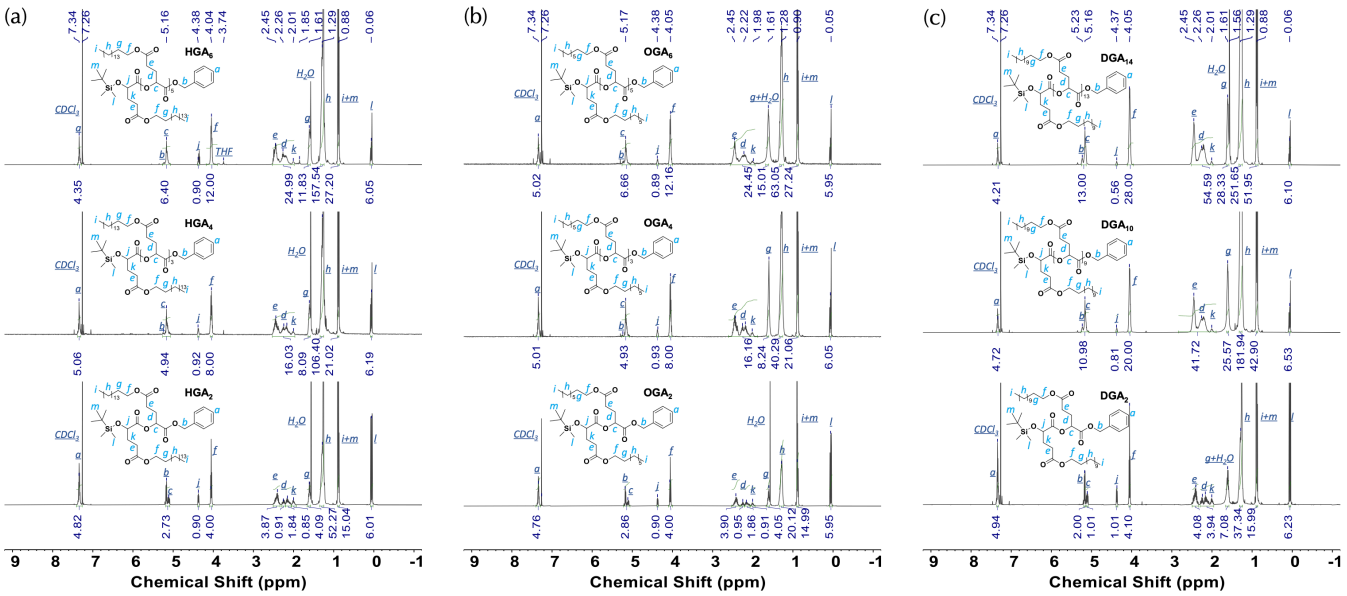

Figure S1. ^{1}H NMR spectra of discrete *o*CGA fragments: (a) H_2, H_4, H_6; (b) O_2, O_4, O_6; (c) D_2, D_{10}, D_{14}.

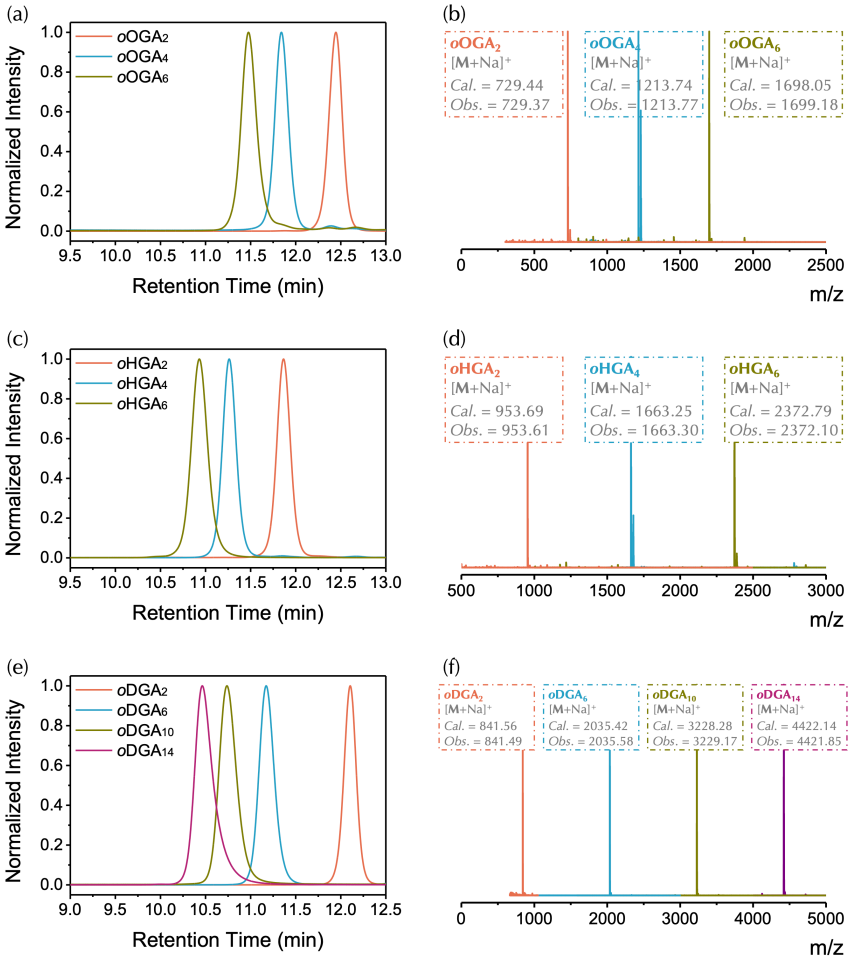

Figure S2. SEC traces (left) and MALDI-ToF MS (right) of discrete *o*CGA fragments: (a-b) O_2, O_4, O_6; (c-d) H_2, H_4, H_6; (e-f) D_2, D_6, D_{10}, D_{14}.

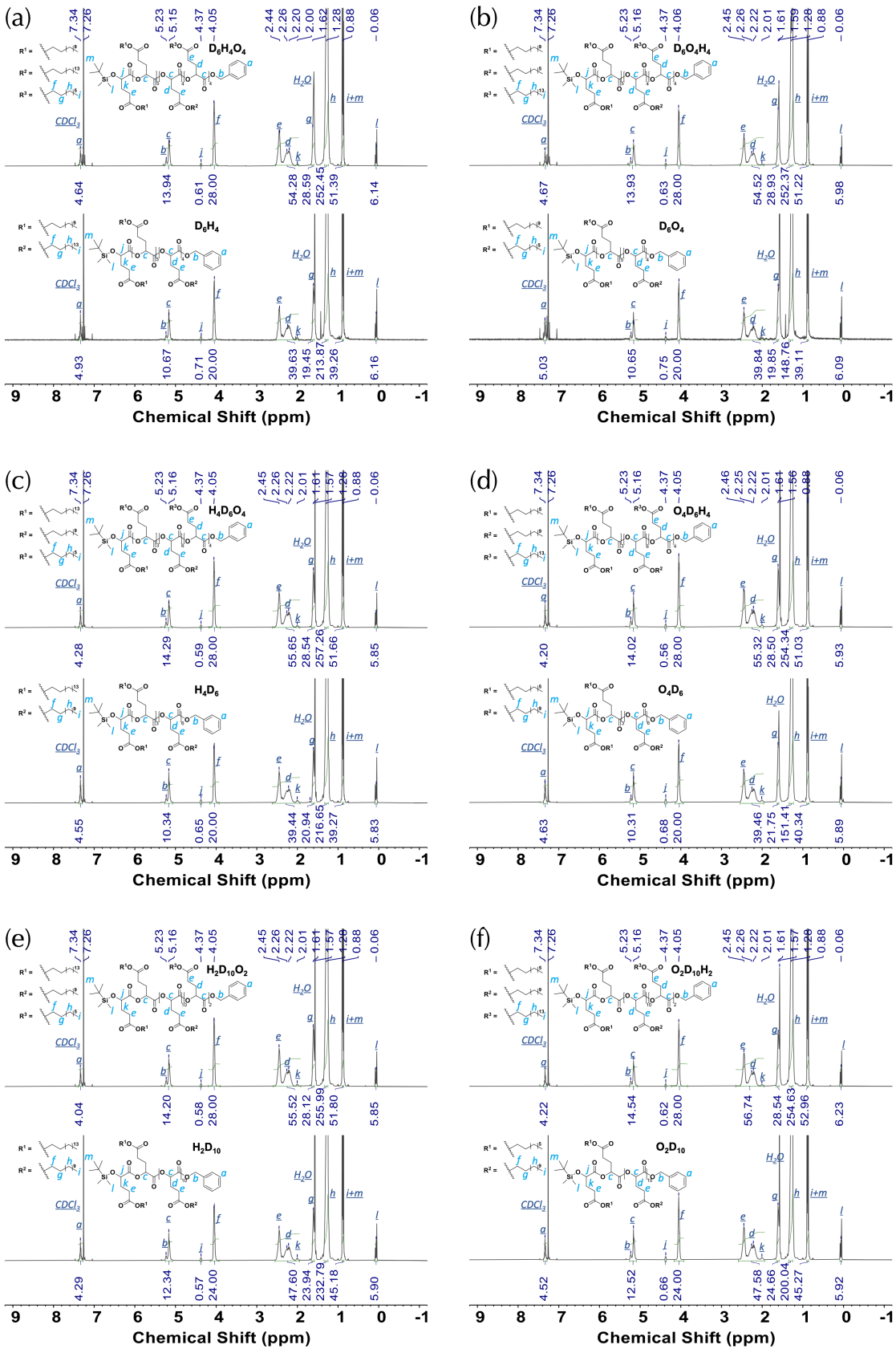

Figure S3. ^{1}H NMR spectra of discrete CGA oligomers with diverse configurations: (a) D_6H_4, $D_6H_4O_4$; (b) D_6O_4, $D_6O_4H_4$; (c) H_4D_6, $H_4D_6O_4$; (d) O_4D_6, $O_4D_6H_4$; (e) H_2D_{10}, $H_2D_{10}O_2$; (f) O_2D_{10}, $O_2D_{10}H_2$.

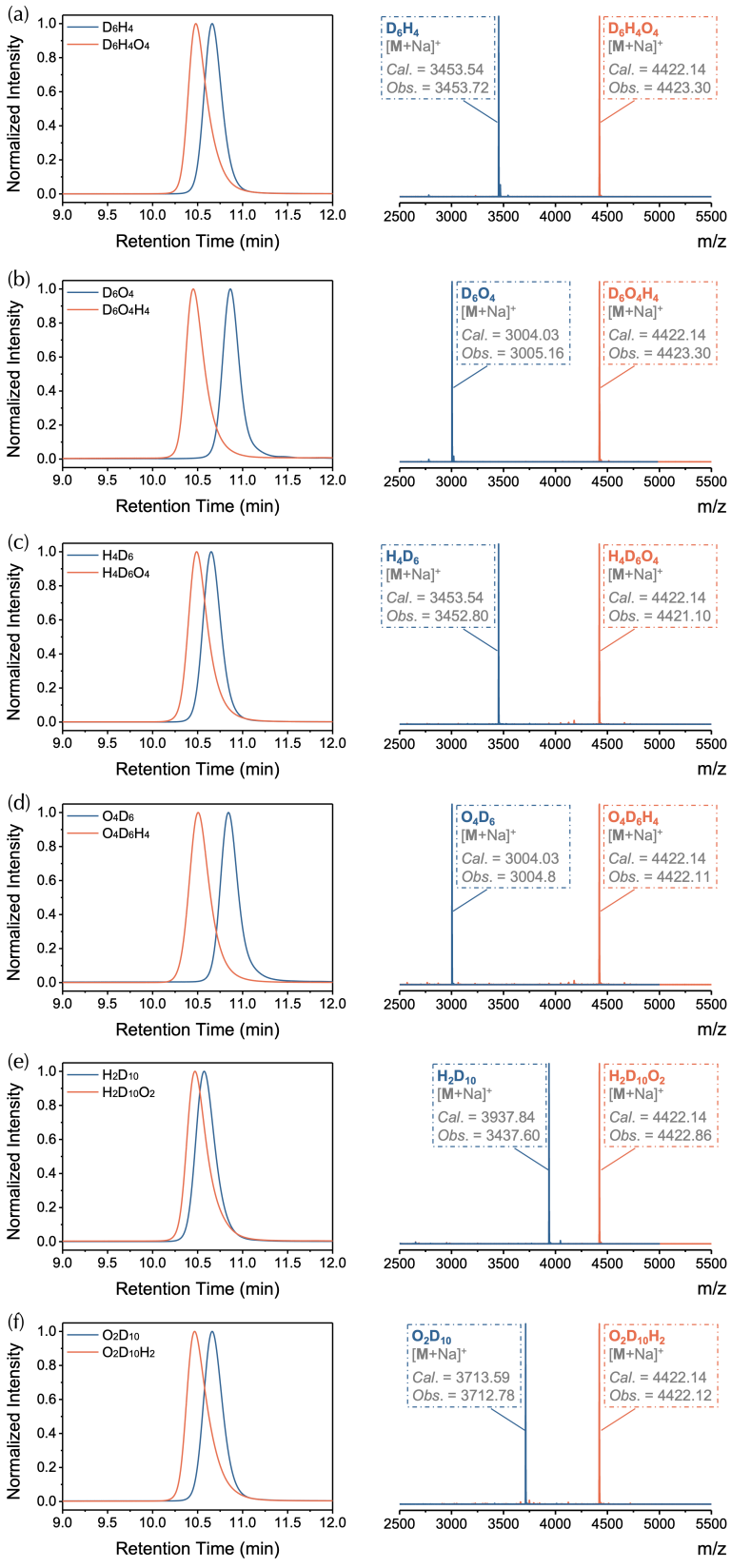

Figure S4. SEC traces (left) and MALDI-ToF MS (right) of discrete CGA oligomers with diverse configurations: (a) D_6H_4, $D_6H_4O_4$; (b) D_6O_4, $D_6O_4H_4$; (c) H_4D_6, $H_4D_6O_4$; (d) O_4D_6, $O_4D_6H_4$; (e) H_2D_{10}, $H_2D_{10}O_2$; (f) O_2D_{10}, $O_2D_{10}H_2$.

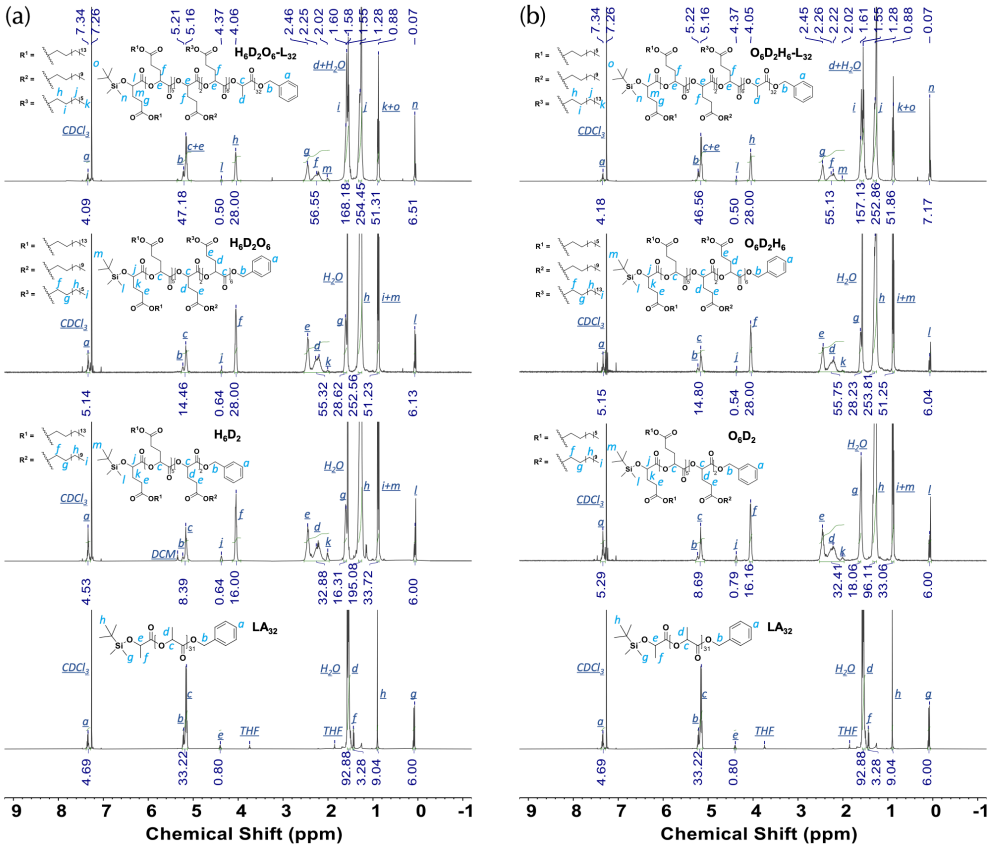

Figure S5. (a) ^{1}H NMR spectra of L_{32}, H_6D_2, $H_6D_2O_6$, and $H_6D_2O_6$-L_{32} (from bottom to top); (b) ^{1}H NMR spectra of L_{32}, O_6D_2, $O_6D_2H_6$, and $O_6D_2H_6$-L_{32} (from bottom to top).

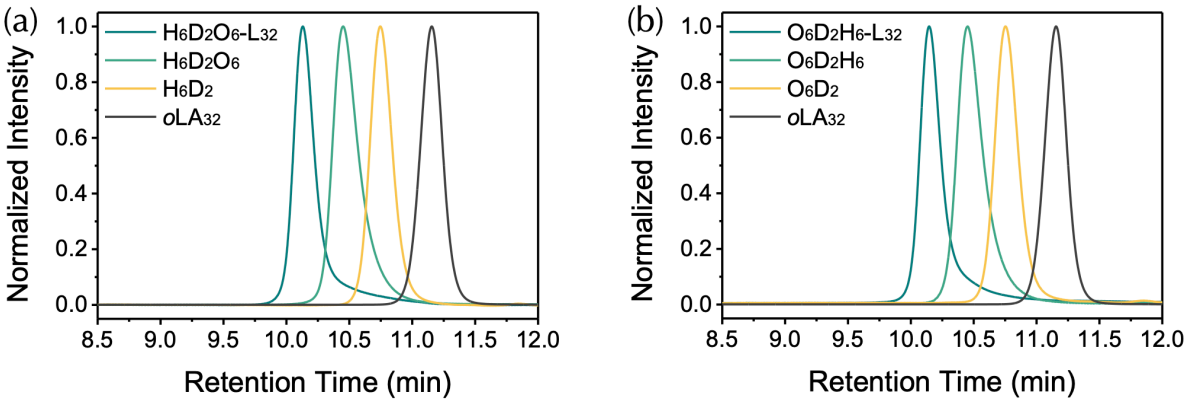

Figure S6. (a) SEC traces of L_{32}, H_6D_2, $H_6D_2O_6$, and $H_6D_2O_6$-L_{32}; (b) SEC traces of L_{32}, O_6D_2, $O_6D_2H_6$, and $O_6D_2H_6$-L_{32}.

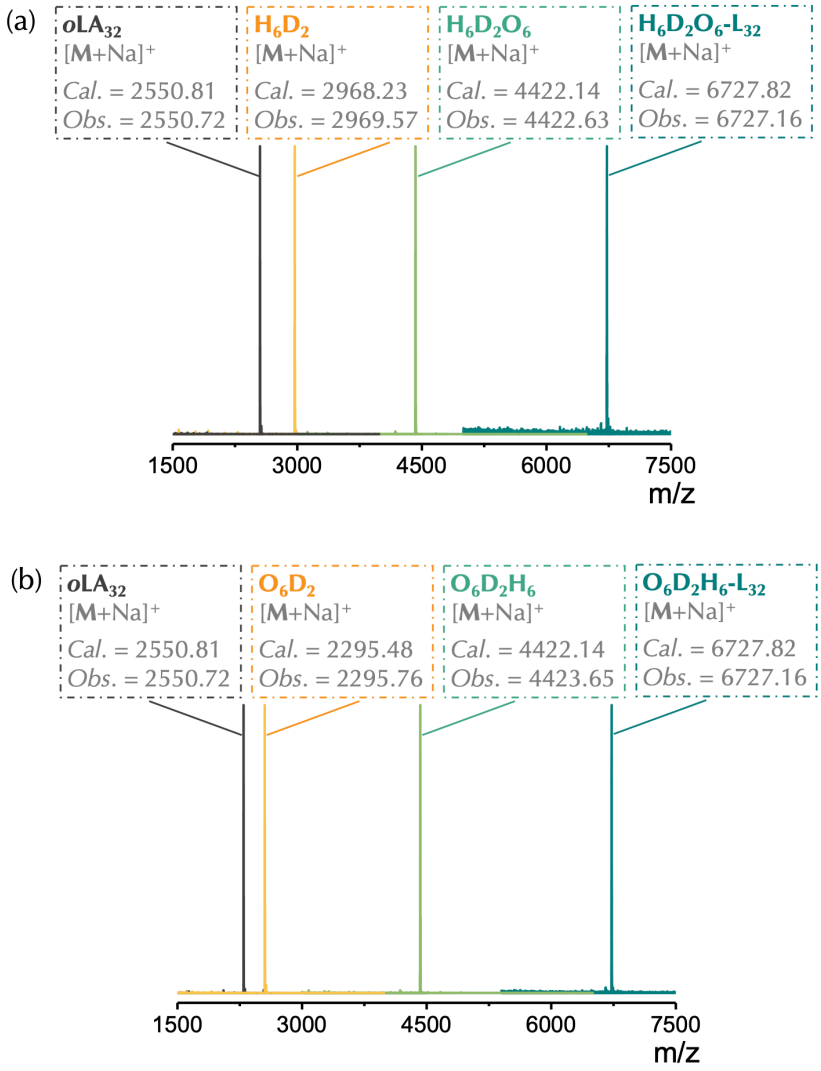

Figure S7. (a) MALDI-ToF MS of L_{32}, H_6D_2, $H_6D_2O_6$, and $H_6D_2O_6$-L_{32}; (b) MALDI-ToF MS of L_{32}, O_6D_2, $O_6D_2H_6$, and $O_6D_2H_6$-L_{32}.

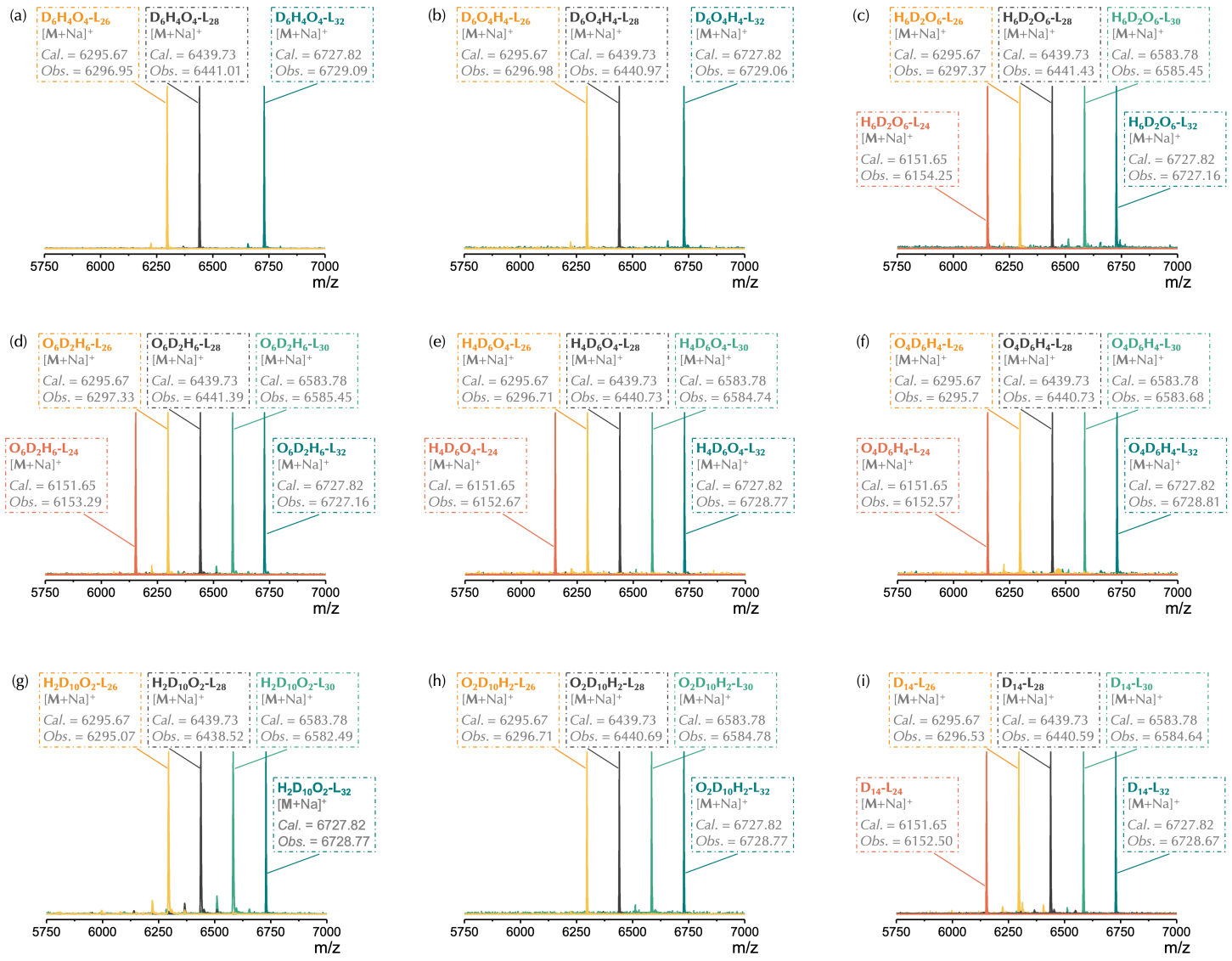

Figure S8. MALDI-ToF MS of discrete diblock polymeric structural isomers: (a) $D_6H_4O_4$-L$_m$; (b) $D_6O_4H_4$-L$_m$; (c) $H_6D_2O_6$-L$_m$; (d) $O_6D_2H_6$-L$_m$; (e) $H_4D_6O_4$-L$_m$; (f) $O_4D_6H_4$-L$_m$; (g) $H_2D_{10}O_2$-L$_m$; (h) $O_2D_{10}H_2$-L$_m$; (i) D_{14}-L$_m$.

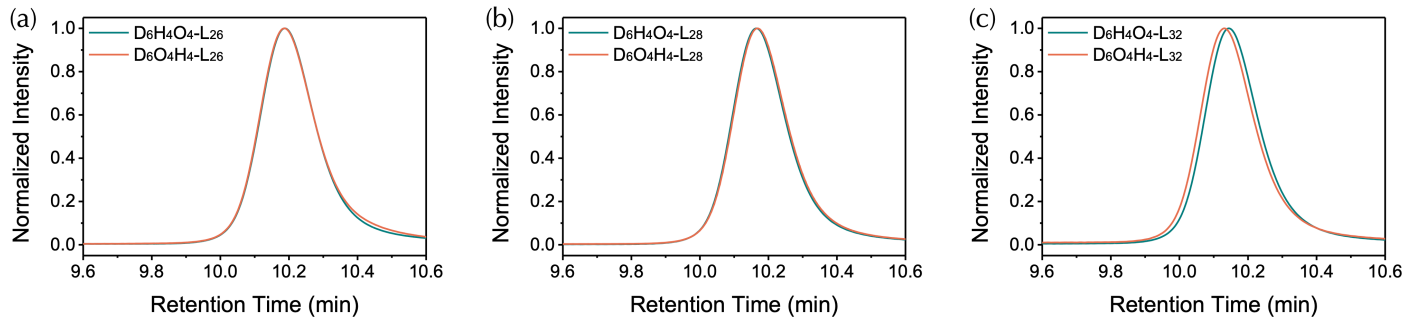

Figure S9. SEC traces of the discrete *o*CGA-*o*LA diblock isomers with non-monotonic gradients $D_6H_4O_4$-L$_m$ and $D_6O_4H_4$-L$_m$: (a) m = 26; (b) m = 28; (c) m = 32.

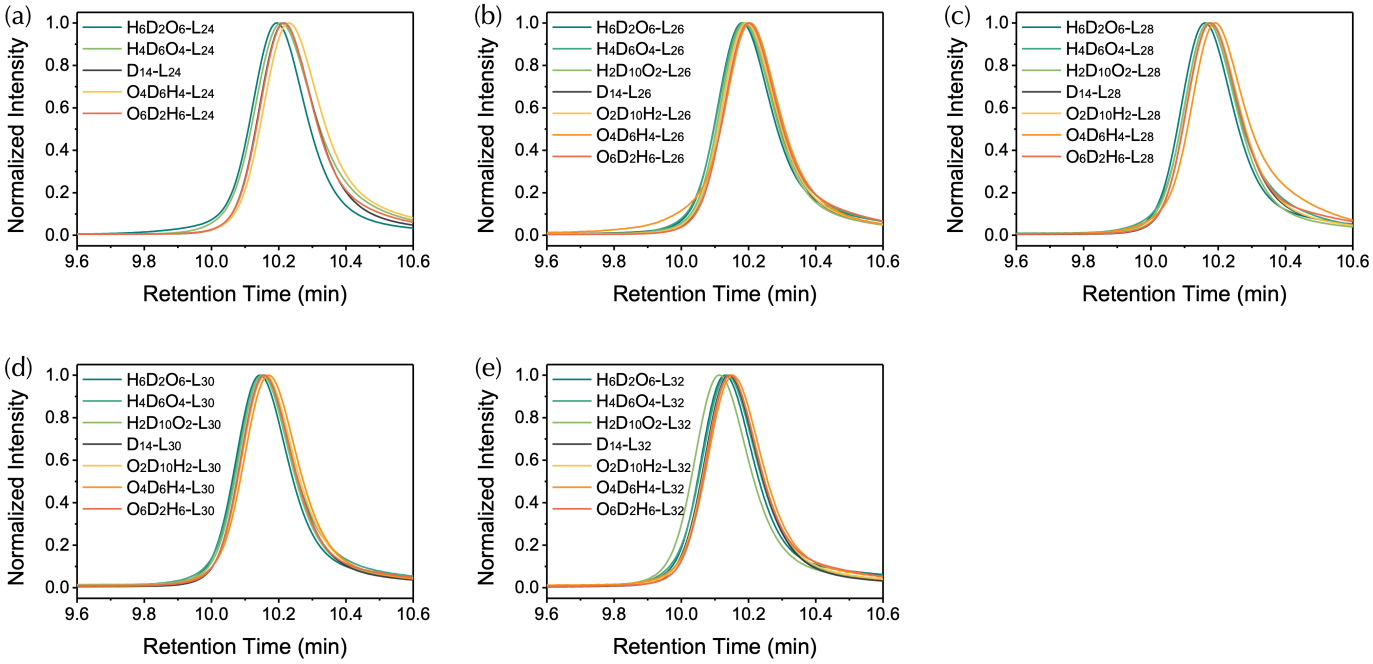

Figure S10. SEC traces of the discrete *o*CGA-*o*LA diblock isomers with monotonic gradients $H_6D_2O_6$-L_m, $H_4D_6O_4$-L_m, $H_2D_{10}O_2$-L_m, D_{14}-L_m, $O_6D_2H_6$-L_m, $O_4D_6H_4$-L_m, and $O_2D_{10}H_2$-L_m: (a) m = 24; (b) m = 26; (c) m = 28; (d) m = 30; (e) m = 32.

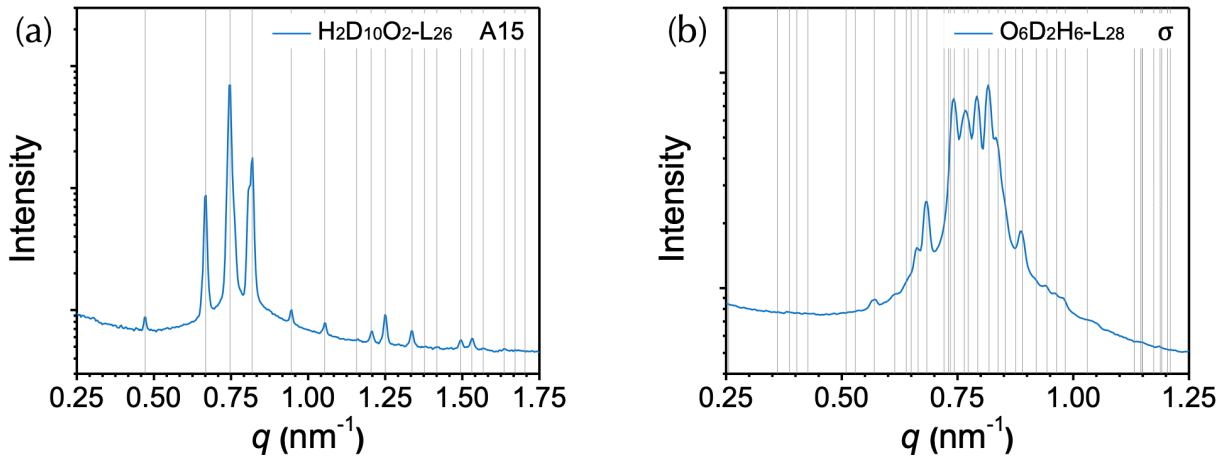

Figure S11. Peak indexing of 1D SAXS profiles of $H_2D_{10}O_2$-L_{26} (a, A15 phase) and $O_6D_2H_6$-L_{28} (b, σ phase). Droplines are the allowed reflections based on the calculated lattice parameter.

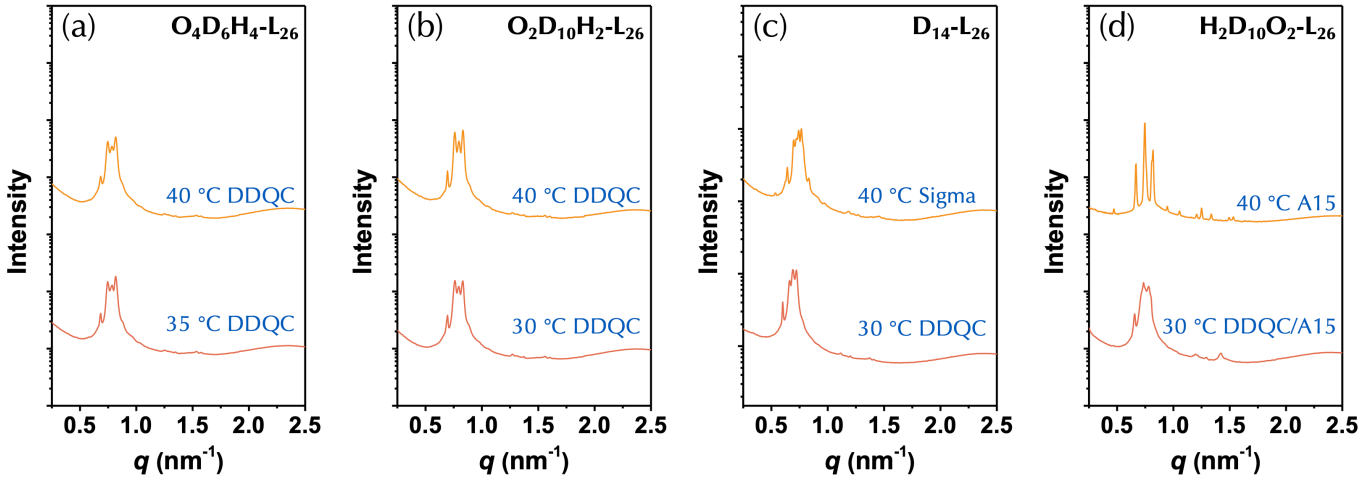

Figure S12. Order-to-order transition: $O_4D_6H_4$-L_{26} (a), $O_2D_{10}H_2$-L_{26} (b), D_{14}-L_{26} (c), and $H_2D_{10}H_2$-L_{26} (d). Samples were annealed at 40 °C for 5 minutes.

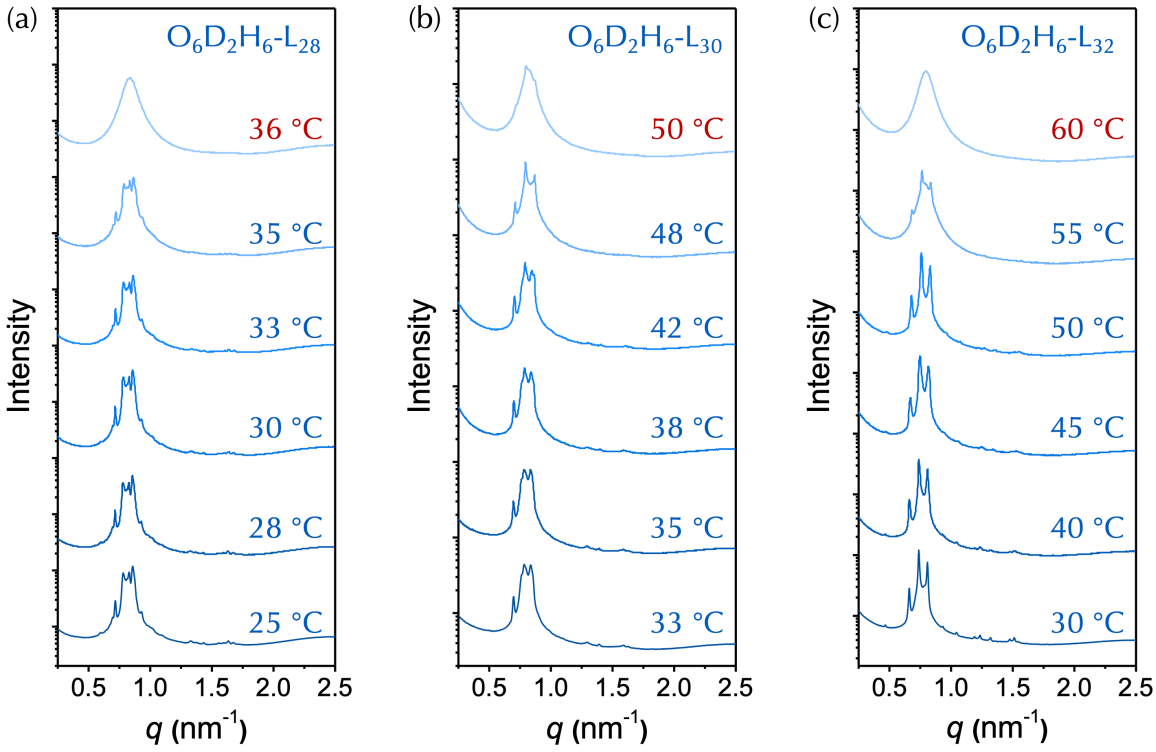

Figure S13. Temperature-dependent SAXS profiles of $O_6D_2H_6$-L_{28} (a), $O_6D_2H_6$-L_{30} (b), and $O_6D_2H_6$-L_{32} (c) (heating rate 10 °C/min). Data are shifted vertically for clarity.

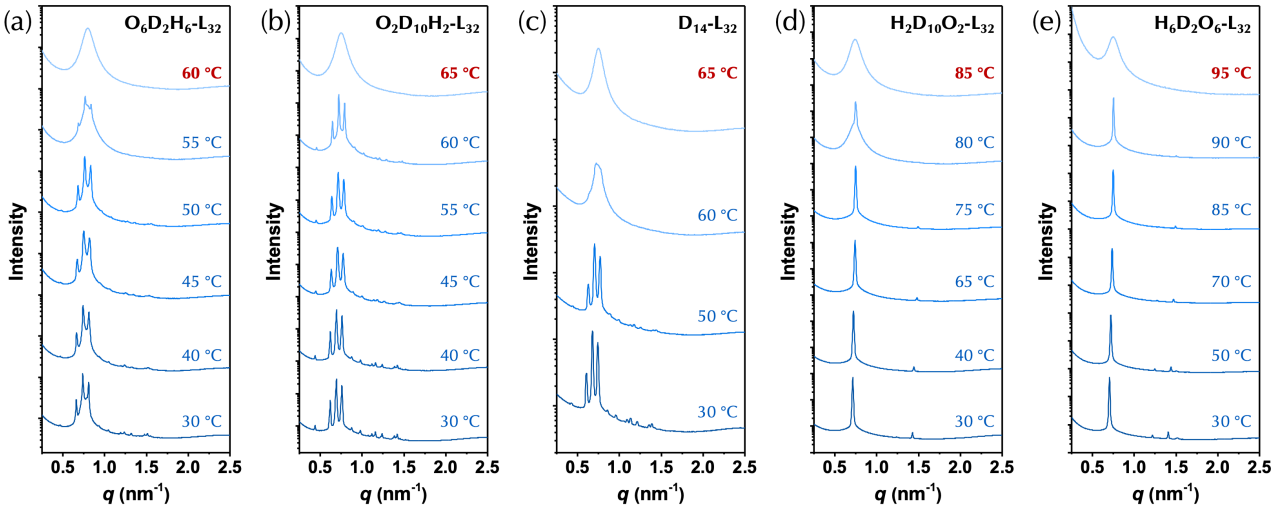

Figure S14. Temperature-dependent SAXS profiles of $O_6D_2H_6$-L_{32} (a), $O_2D_{10}H_2$-L_{32} (b), D_{14}-L_{32} (c), $H_2D_{10}O_2$-L_{32} (d), and $H_6D_2O_6$-L_{32} (e) (heating rate 10 °C/min). Data are shifted vertically for clarity.

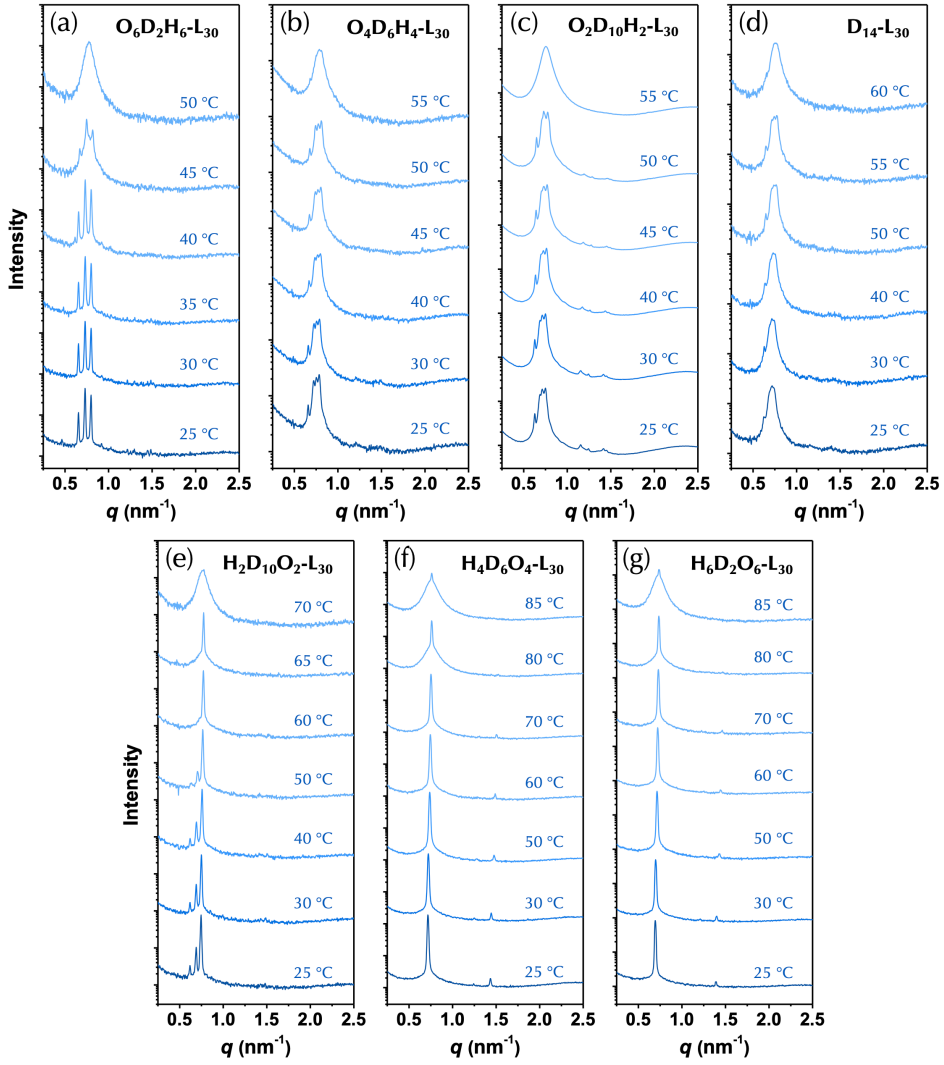

Figure S15. Temperature-dependent SAXS profiles of $O_6D_2H_6$-L_{30} (a), $O_4D_6H_4$-L_{30} (b), $O_2D_{10}H_2$-L_{30} (c), D_{14}-L_{30} (d), $H_2D_{10}O_2$-L_{30} (e), $H_4D_6O_4$-L_{30} (f), and $H_6D_2O_6$-L_{30} (g) (heating rate 10 °C/min). Data are shifted vertically for clarity.

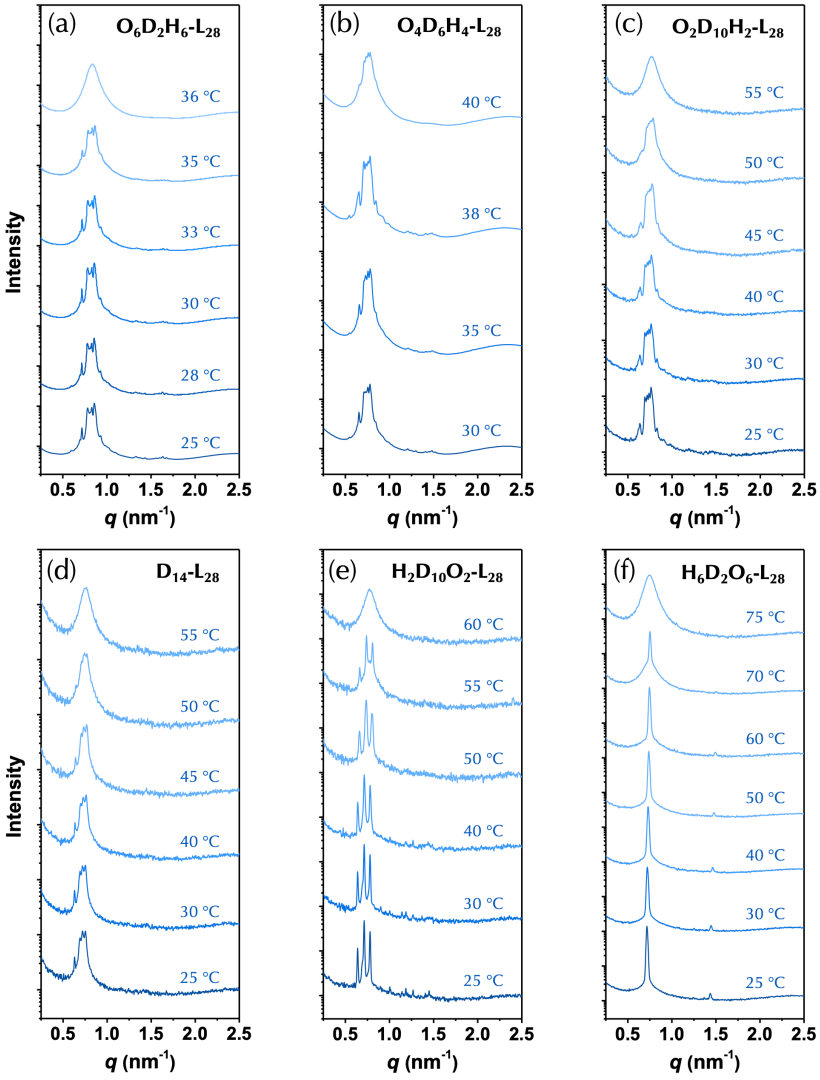

Figure S16. Temperature-dependent SAXS profiles of $O_6D_2H_6$-L_{28} (a), $O_4D_6H_4$-L_{28} (b), $O_2D_{10}H_2$-L_{28} (c), D_{14}-L_{28} (d), $H_2D_{10}O_2$-L_{28} (e), and $H_6D_2O_6$-L_{28} (f) (heating rate 10 °C/min). Data are shifted vertically for clarity.

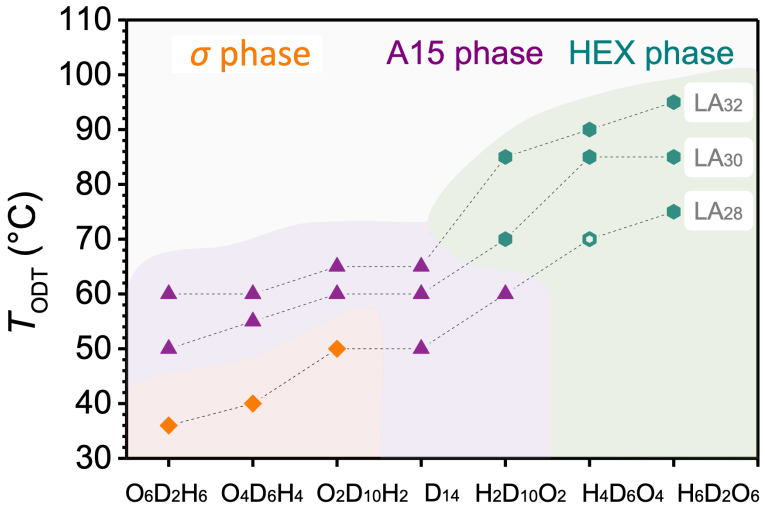

Figure S17. Variation of T_{ODT} of the isomeric block polymers.

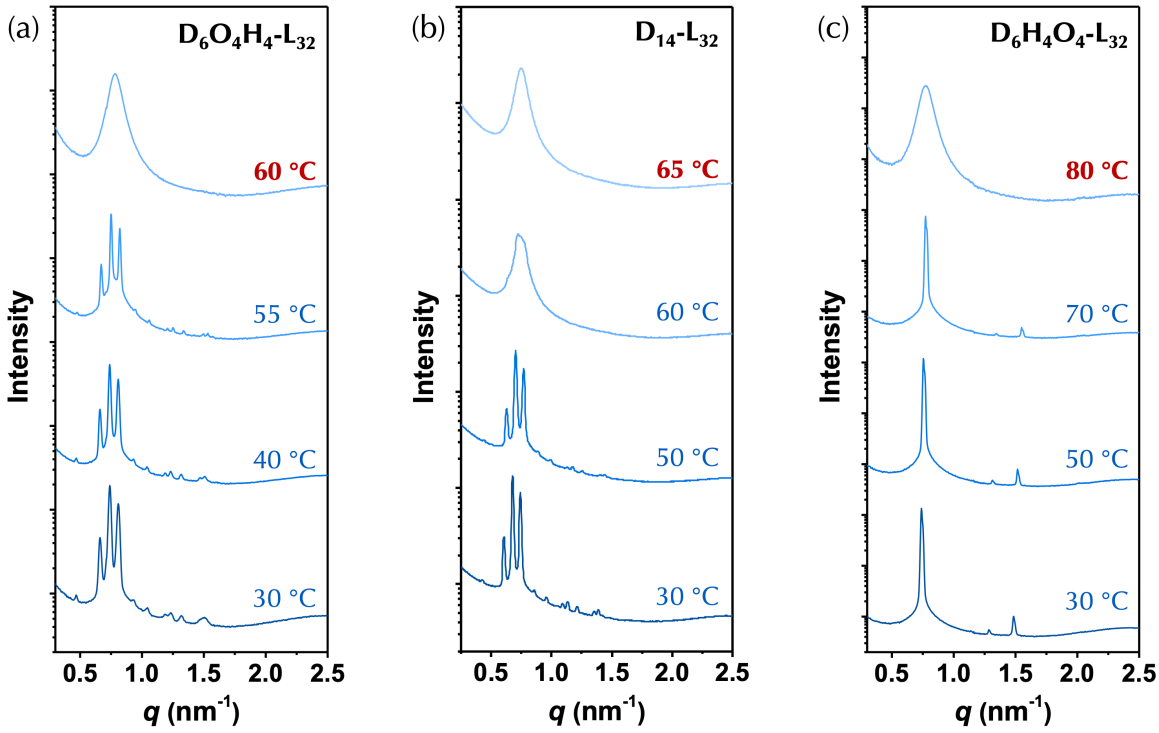

Figure S18. Temperature-dependent SAXS profiles of $D_6O_4H_4$-L_{32} (a), D_{14}-L_{32} (b), and $D_6H_4O_4$-L_{32} (c) (heating rate 10 °C/min). Data are shifted vertically for clarity.

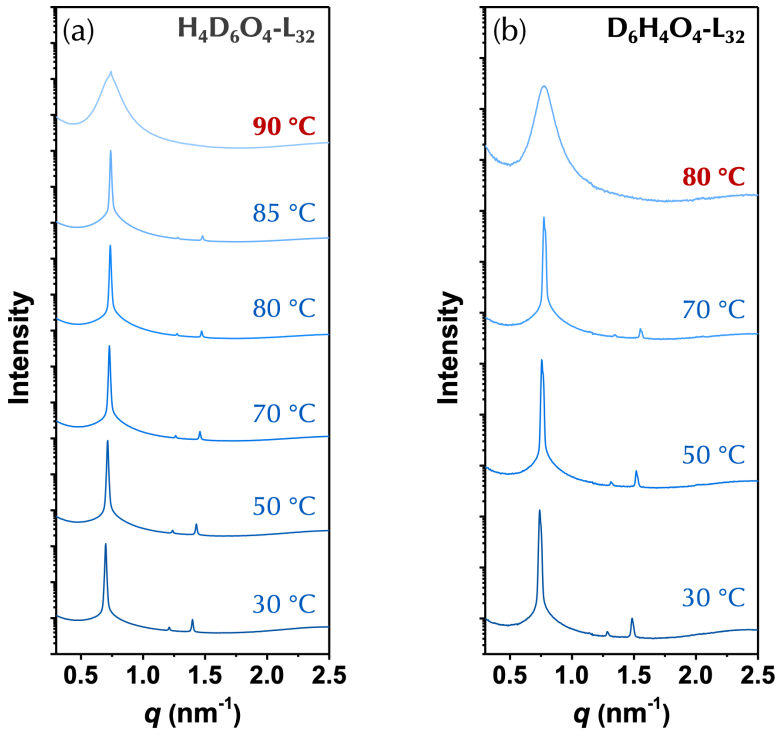

Figure S19. Temperature-dependent SAXS profiles of $H_4D_6O_4$-L_{32} (a), and $D_6H_4O_4$-L_{32} (b) (heating rate 10 °C/min). Data are shifted vertically for clarity.

(1) Tan, R.; Zhou, D.; Liu, B.; Sun, Y.; Liu, X.; Ma, Z.; Kong, D.; He, J.; Zhang, Z.; Dong, X.-H. Precise modulation of molecular weight distribution for structural engineering. *Chem. Sci.* **2019**, *10* (46), 10698-10705. DOI: 10.1039/C9SC04736K.

(2) Sun, Y.; Tan, R.; Ma, Z.; Gan, Z.; Li, G.; Zhou, D.; Shao, Y.; Zhang, W. B.; Zhang, R.; Dong, X. H. Discrete Block Copolymers with Diverse Architectures: Resolving Complex Spherical Phases with One Monomer Resolution. *ACS Cent. Sci.* **2020**, *6* (8), 1386-1393. DOI: 10.1021/acscentsci.0c00798.

(3) Zhou, D.; Xu, M.; Ma, Z.; Gan, Z.; Tan, R.; Wang, S.; Zhang, Z.; Dong, X. H. Precisely Encoding Geometric Features into Discrete Linear Polymer Chains for Robust Structural Engineering. *J. Am. Chem. Soc.* **2021**, *143* (44), 18744-18754. DOI: 10.1021/jacs.1c09575.